

# A Study on the Role of Electric Field in Low-Temperature Plasma Catalytic Ammonia Synthesis via Integrated Density Functional Theory and Microkinetic Modeling

Ketong Shao and Ali Mesbah\*



Cite This: *JACS Au* 2024, 4, 525–544



Read Online

ACCESS |

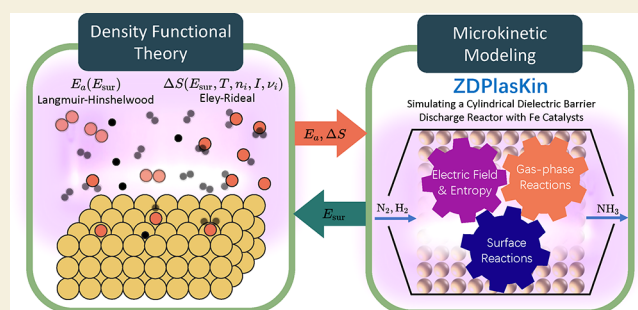
Metrics & More

Article Recommendations

Supporting Information

**ABSTRACT:** Low-temperature plasma catalysis has shown great promise for various chemical processes such as light hydrocarbon conversion, volatile organic compounds removal, and ammonia synthesis. Plasma-catalytic ammonia synthesis has the potential advantages of leveraging renewable energy and distributed manufacturing principles to mitigate the pressing environmental challenges of the energy-intensive Haber-Bosch process, towards sustainable ammonia production. However, lack of foundational understanding of plasma-catalyst interactions poses a key challenge to optimizing plasma-catalytic processes. Recent studies suggest electro- and photoeffects, such as electric field and charge, can play an important role in enhancing surface reactions. These studies mostly rely on using density functional theory (DFT) to investigate surface reactions under these effects. However, integration of DFT with microkinetic modeling in plasma catalysis, which is crucial for establishing a comprehensive understanding of the interplay between the gas-phase chemistry and surface reactions, remains largely unexplored. This paper presents a first-principles framework coupling DFT calculations and microkinetic modeling to investigate the role of electric field on plasma-catalytic ammonia synthesis. The DFT-microkinetic model shows more consistent predictions with experimental observations, as compared to the case wherein the variable effects of plasma process parameters on surface reactions are neglected. In particular, predictions of the DFT-microkinetic model indicate electric field can have a notable effect on surface reactions relative to other process parameters. A global sensitivity analysis is performed to investigate how ammonia synthesis pathways will change in relation to different plasma process parameters. The DFT-microkinetic model is then used in conjunction with active learning to systematically explore the complex parameter space of the plasma-catalytic ammonia synthesis to maximize the amount of produced ammonia while inhibiting reactions dissipating energy, such as the recombination of  $H_2$  through gas-phase H radicals and surface-adsorbed H. This paper demonstrates the importance of accounting for the effects of electric field on surface reactions when investigating and optimizing the performance of plasma-catalytic processes.

**KEYWORDS:** Plasma catalysis,  $NH_3$  synthesis, density functional theory, microkinetic modeling, global sensitivity analysis, active learning, multiobjective Bayesian optimization



## INTRODUCTION

Sustainable processes for nitrogen fixation and fertilizer production are urgently needed to meet the food demands of a rapidly growing world population.<sup>1,2</sup> Industrial-scale ammonia ( $NH_3$ ) production almost exclusively relies on the Haber-Bosch (H-B) process, which is essential for the manufacture of synthetic fertilizer supporting nearly 50% of the world population.<sup>3,4</sup> The H-B process is a thermal catalytic process under high pressure (100 to 400 atm) and high temperature (700 to 800 K), using  $H_2$  feedstock produced via  $CH_4$  reforming.<sup>5,6</sup> As such, the H-B process is excessively energy-intensive and leads to significant green-house gas emissions. Although the H-B process has been extensively optimized since its invention in 1905, with a current energy consumption of 27 GJ/tN (gigajoules expended per metric ton nitrogen converted)

approaching its theoretical limit of 23 GJ/tN,<sup>7</sup> it consumes 1% to 2% of the world's annual energy production.<sup>8</sup>

To find more sustainable and greener alternatives for nitrogen fixation, recent years have witnessed significant efforts in electrocatalytic,<sup>9</sup> photoelectrochemical,<sup>10</sup> and low-temperature plasma (LTP) processes.<sup>11,12</sup> This work focuses on nitrogen fixation via LTP, which has attracted increasing attention since

**Received:** October 26, 2023

**Revised:** December 14, 2023

**Accepted:** December 18, 2023

**Published:** January 16, 2024



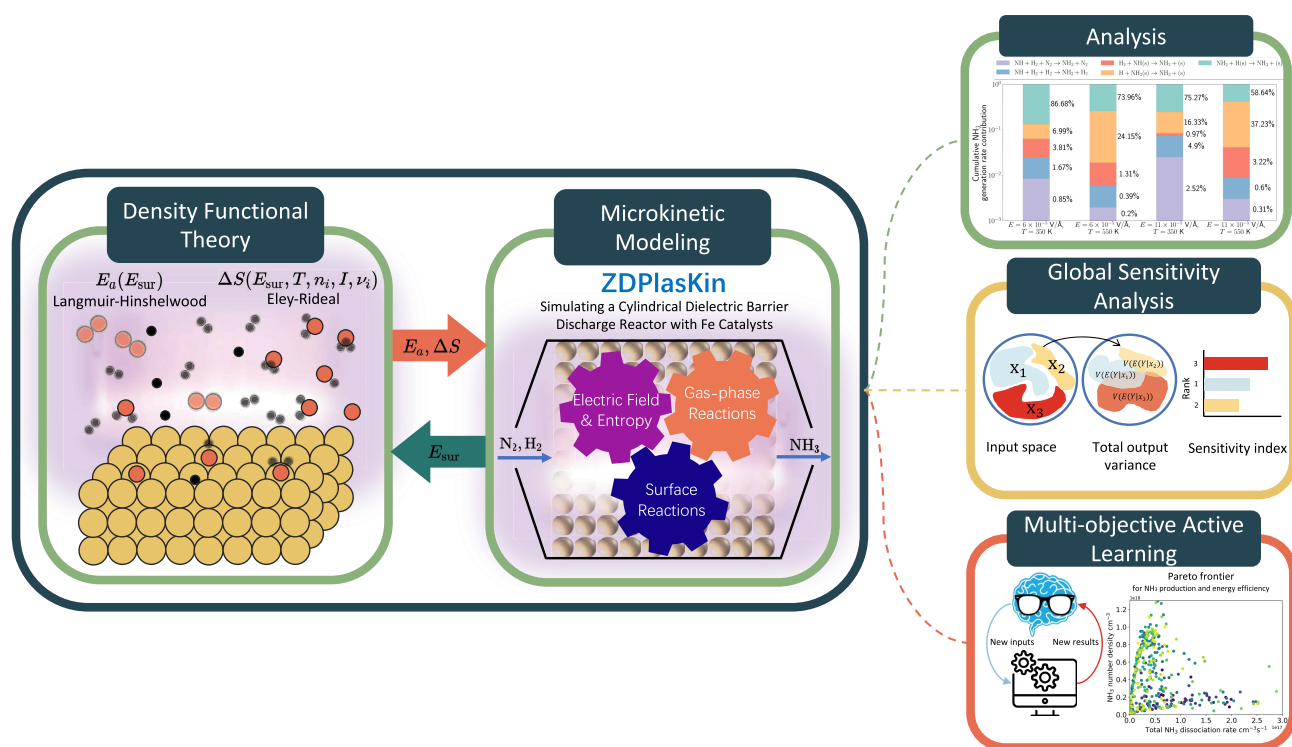


**Figure 1.** Integrated DFT-microkinetic model and the analysis conducted in this paper. The integrated model accounts for the synergistic plasma-catalyst effects that stem from variations in electric field, activation energies (L-H reactions), and entropies (E-R reactions). The model is used to perform the following studies: 1. establish the impacts of electric field and gas temperature on the generation and loss of gas-phase and surface species; 2. quantify the contribution of each process parameter on the main quantities of interest such as  $\text{NH}_3$  concentration and surface reaction rates via a global sensitivity analysis; and 3. investigate the trade-off between  $\text{NH}_3$  production and energy efficiency via multiobjective active learning.

$\text{NH}_3$  synthesis can be performed under atmospheric pressure and low temperatures.<sup>12,13</sup> The high-energy electrons in LTPs can lead to vibrational excitation and/or chemical bond breaking of molecules.<sup>14</sup> Therefore, LTP-assisted nitrogen fixation can, in principle, have a lower theoretical energy cost limit than that of the H-B process.<sup>15,16</sup> Additionally, electricity is the main energy input to LTP processes, making LTP-assisted nitrogen fixation a green process when renewable electricity is used.

Although LTP-assisted  $\text{NH}_3$  synthesis can be performed without catalysis, it has been shown that the addition of heterogeneous catalysts can significantly reduce the energy cost of  $\text{NH}_3$  synthesis.<sup>17–19</sup> This is attributed to the complex and not-well-understood synergies between the LTP and catalyst.<sup>20,21</sup> Several studies have been conducted to investigate the synergistic plasma-catalyst effects by leveraging physics-based simulation tools, such as density functional theory (DFT) and microkinetic models, as well as experiments in LTP-assisted catalytic reactors.<sup>22–26</sup> Liu et al.<sup>27</sup> employed DFT calculations to study various possible surface reactions, including Eley-Rideal (E-R), Langmuir-Hinshelwood (L-H), and radical adsorption and dissolution, on nine different types of metallic catalyst surfaces. A possible pathway for ammonia synthesis was established that involves the formation of NNH from radical reactions. In addition, it was found that N radicals are likely the main source of nitrogen for  $\text{NH}_3$  production, while E-R hydrogenation is the primary hydrogenation pathway. However, the DFT calculations in ref 27 were performed without accounting for any surface factors, such as electric field. Hong et al.<sup>25</sup> developed a 0-dimensional (0D) microkinetic model with surface reactions using ZDPlasKin,<sup>28</sup> which was experimentally validated for plasma-catalytic ammonia synthesis in a

dielectric barrier discharge (DBD) reactor with  $\text{Al}_2\text{O}_3$ , nano-diamond-coated alumina, and metallic catalysts. This 0D microkinetic model enabled investigation of some of the main  $\text{NH}_3$  production pathways and their associated key surface reactions. Nevertheless, the microkinetic model used in ref 25 did not account for the effects of surface factors, such as electric field and charge on the surface reactions, thus neglecting plasma-catalyst interactions. Mehta et al.<sup>17</sup> developed a microkinetic model in which the vibrational excitation of  $\text{N}_2$  was informed by DFT calculations, which in turn influenced the subsequent dissociative adsorptions. It was found that the optimal catalyst for achieving high reaction rates in plasma-catalytic processes can differ from the catalysts used in thermal catalysis due to a weaker binding of nitrogen. Engelmann et al.<sup>29</sup> investigated the role of the E-R reactions manipulated by entropic barriers via microkinetic modeling. This study revealed that E-R reactions can reduce the dependence of turnover frequency on the catalyst binding energy, particularly for less noble catalysts.

Despite significant work on understanding plasma-catalyst interactions, the underpinning mechanisms of surface reactions in the presence of plasma remain largely elusive.<sup>30,31</sup> It has been shown that catalyst surface geometry, surface electric field, and accumulated electrons can influence surface reactions,<sup>24,31,32</sup> but how surface reactions are impacted by these factors is still unclear. To this end, a key challenge arises from limited diagnostics of surface reactions in the presence of plasma,<sup>26</sup> even though there have been recent studies on *in situ* spectroscopic diagnostics of intermediate species during plasma-catalytic ammonia synthesis.<sup>33,34</sup> On the other hand, first-principles calculations such as DFT that can shed useful insights onto plasma–surface interactions are particularly expensive, espe-

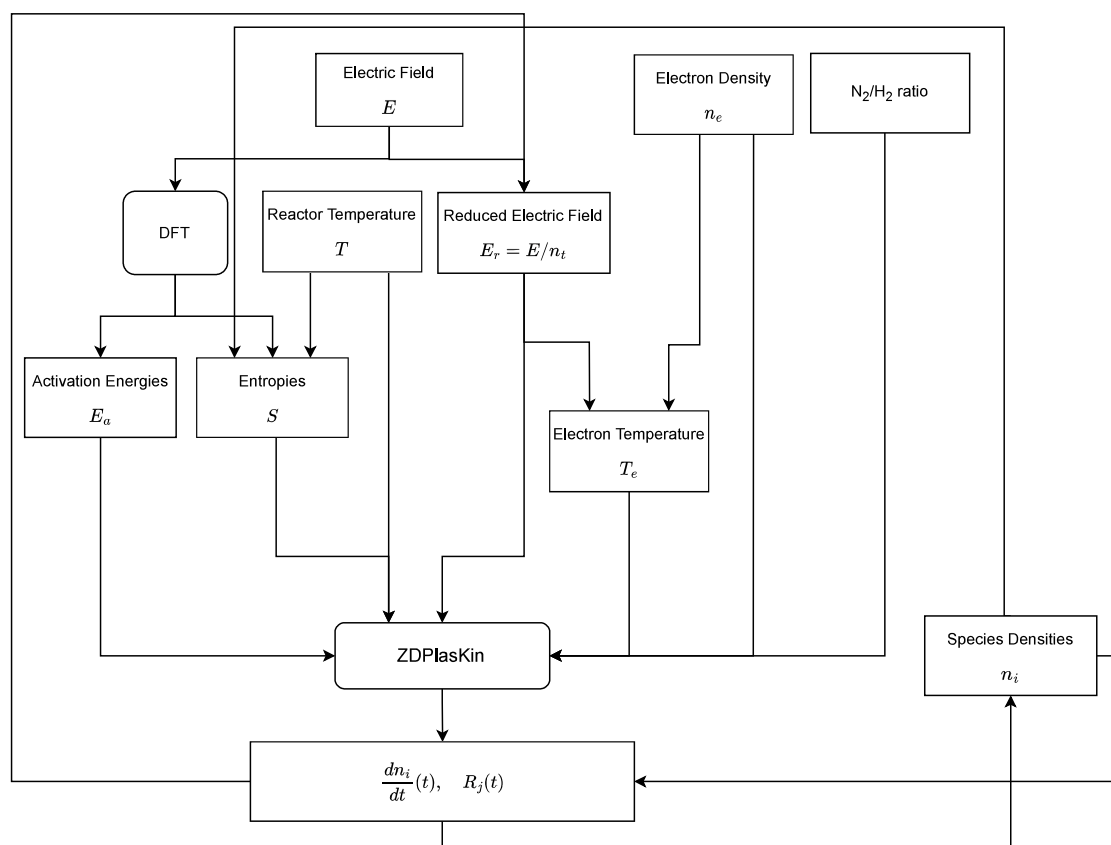


**Figure 2.** 0D microkinetic model of a packed-bed dielectric barrier discharge coupled with first-principles DFT calculations. The model accounts for the impact of surface electric field on plasma-catalyst interactions in plasma-assisted ammonia synthesis using Fe(110) catalyst. Electric field  $E$ , electron density  $n_e$ , inlet gas  $N_2/H_2$  ratio, and reactor temperature  $T$  can be manipulated.

cially when accounting for electric field and charged species that are central to the synergistic plasma-catalyst effects. These challenges have impaired the development and optimization of plasma-catalytic processes for ammonia synthesis.

In this paper, we investigate the impact of electric field, in combination with other plasma process parameters, on LTP-assisted catalytic synthesis of  $NH_3$  (see Figure 1). The 0D microkinetic model of Hong et al.<sup>25</sup> is adapted with surface reactions that can respond to varying levels of electric field. While maintaining the cylindrical DBD reactor geometry used in ref 25, we substitute  $Al_2O_3$  pellets with Fe(110) catalyst. The choice of Fe(110) is motivated by its stability, being the most stable facet of the body-centered cubic metal. Moreover, there is extensive literature on Fe(110) concerning its adsorption energies for different molecules.<sup>35</sup> Fe is also proven to be an exemplary monometallic catalyst for thermal ammonia synthesis, as evidenced by multiple studies,<sup>36–38</sup> and is the subject of significant research for plasma-catalytic ammonia synthesis,<sup>17,39,40</sup> providing an extensive basis for comparison.<sup>a</sup> Notably, we investigate how the rate coefficients of the surface reactions, including adsorption, L-H, and E-R reactions, are influenced by changes of electric field on the catalyst surface. Electric field can influence activation energies, thereby manipulating L-H reactions. For E-R reactions, a new approach is proposed to incorporate electric field into the calculation of sticking probabilities, while leveraging the widely used E-R reaction rate coefficient expressions as in refs 25 and 41. The sticking probabilities of the E-R reactions are considered to be controlled by the reaction entropy changes, which are a function of electric field. DFT is utilized to calculate activation energies

and species entropies under different levels of electric field. Polynomial models are then fitted to interpolate the activation energies and entropies, which are utilized in the microkinetic model to describe the plasma-catalyst interactions in relation to varying levels of electric field.

In the **Methods** section, we first present a detailed overview of the 0D microkinetic model, followed by a description of rate coefficients for surface reactions and their proposed adaptations to account for surface electric field. In addition, we introduce utilization of the Fe(110) structure and how electric field is incorporated into the DFT calculations. In the **Results and Discussion** section, we study the impact of electric field and other parameters of the plasma-catalytic process. First, we conduct simulations under two levels of electric field and gas temperature (equal to the catalyst temperature) to assess their influence on gas-phase and surface species, as well as on surface reactions. The calculations of L-H and E-R reaction rate coefficients, as well as sticking probabilities, heavily depend on both the electric field and gas temperature. Accordingly, we observe notable effects on the key reaction rates and concentration of gas-phase and surface species, leading to different reaction pathways for plasma-catalytic synthesis of  $NH_3$ .

To systematically quantify the contribution of all process parameters to important quantities of interest such as  $NH_3$  concentration and surface reaction rates, we perform a global sensitivity analysis, which reveals that electric field can have a significant, yet variable, influence on different reaction rates. This analysis suggests that the surface electric field affects the  $NH_3$  synthesis pathways and energy consumption in a nonlinear

and nontrivial manner. Finally, we employ an active learning strategy<sup>46</sup> based on multiobjective Bayesian optimization<sup>42–46</sup> to explore the trade-off between reactions dissipating energy and producing NH<sub>3</sub>, with the goal of determining the “optimal” process parameters that minimize energy consumption while maximizing the NH<sub>3</sub> concentration.

## METHODS

The microkinetic model coupled with DFT used in this work is shown in Figure 2. In this framework, the microkinetic model takes in as inputs the plasma process parameters, namely, temperature  $T$ , reduced electric field  $E_r$ , electron density  $n_e$ , and inlet N<sub>2</sub>/H<sub>2</sub> ratio, to simulate the plasma-catalytic NH<sub>3</sub> synthesis process. DFT calculations provide energies and entropies required for determining, respectively, the rate coefficients of L-H and E-R surface reactions under a given surface electric field strength on Fe(110). The surface electric field strength is inferred from  $E_r$  and the total number density of species in the gas phase  $n_t$ . Since reaction entropies also depend on the temperature and partial pressure of species in the gas phase, entropies are updated in every time step of the microkinetic model simulation. As species densities also change at each simulation time step, the surface electric field is recalculated and is fed into a polynomial model trained using data from DFT calculations to obtain the new energies and entropies. Each part of the modeling framework of Figure 2 is discussed in the following subsections. The notation used throughout this paper is given in the *Nomenclature* section.

### Microkinetic Model

In this work, the reactor is a cylindrical packed-bed type DBD reactor, where the discharge is assumed to be uniform, and its volume is 48.6 cm<sup>3</sup>. The catalyst consists of 1.6 mm Fe spheres, leading to a geometric surface area of 3370 cm<sup>2</sup>. A roughness factor of 2.1 is used for the catalyst, yielding a volume to area ratio of 0.00687 cm. In the DFT calculations, the surface is assumed to be flat Fe(110). ZDPlasKin<sup>28</sup> is used as the 0D kinetics solver, where the Boltzmann equation is solved via BOLSIG+<sup>47</sup> for reactions involving electrons. A graphical interface program, QTPlasKin,<sup>48</sup> is used to process the output files from ZDPlasKin for further analysis. The microkinetic model is comprised of the gas-phase and surface reactions. The set of reactions and species, as well as the reactor geometry, are taken from Hong et al.,<sup>25</sup> however, the surface reactions are modified to account for the effect of surface electric field.

ZDPlasKin solves the following mass conservation balance for each species

$$\frac{dn_i}{dt} = \sum_{j=1}^{j_{\max}} Q_{ij}(t) \quad (1)$$

where  $n_i$  is the number density for the  $i^{\text{th}}$  species,  $j_{\max}$  is the total number of reactions involving the  $i^{\text{th}}$  species, and  $Q_{ij}(t)$  is the reaction rate of production/consumption of this species by the  $j^{\text{th}}$  reaction per unit volume. The different types of species considered in this work are listed in Table 1. It should be noted that NH<sub>3</sub>(s) only appears in the DFT calculations for activation energy and entropy barrier calculations.

In the DFT-microkinetic model, gas temperature  $T$ , electron number density  $n_e$ , electric field  $E$ , and N<sub>2</sub> volume fraction in the inlet mixture of N<sub>2</sub> and H<sub>2</sub> can be manipulated. The chosen ranges for these four process parameters are given in Table 2, which are the same as those used in refs 25 and 49. The gas temperature is assumed to be the same as the surface temperature. The gas temperature range is 300–600 K because DBDs usually have a low discharge temperature.<sup>17,25,50,51</sup> The electron number density and the electric field strength are considered as averaged quantities in the DBD.<sup>25,49</sup> According to refs 52 and 53, the strength of electric field in the gas phase is within the range of 10<sup>–5</sup> to 10<sup>–4</sup> V/Å, as also used in ref 25. In ZDPlasKin, electric field is not an input. Reduced electric field  $E_r$  is used as an input by the BOLSIG+ solver to calculate electron interactions.<sup>28,47</sup> Here, the resulting reduced electric field  $E_r$  is within the range of 30–100 Td, which is consistent with typical values reported for DBD reactors.<sup>52,54</sup> In addition, the

**Table 1. Species Considered in the Microkinetic Model**

Ground-state molecules	N <sub>2</sub> , H <sub>2</sub> , NH <sub>3</sub>
Vibrationally excited molecules	N <sub>2</sub> ( $\nu = 1, \dots, 8$ ), H <sub>2</sub> ( $\nu = 1, 2, 3$ )
Electronically excited molecules	N <sub>2</sub> (A3), N <sub>2</sub> (B3), N <sub>2</sub> (a'1), N <sub>2</sub> (C3), H <sub>2</sub> (B3), H <sub>2</sub> (B1), H <sub>2</sub> (C3), H <sub>2</sub> (A3), H <sub>2</sub> (R)
Radicals	N, N(2D), N(2P), H, NH, NH <sub>2</sub>
Ions	N <sup>+</sup> , N <sub>2</sub> <sup>+</sup> , N <sub>3</sub> <sup>+</sup> , N <sub>4</sub> <sup>+</sup> , H <sup>+</sup> , H <sub>2</sub> <sup>+</sup> , H <sub>3</sub> <sup>+</sup> , H <sup>–</sup> , NH <sup>+</sup> , N <sub>2</sub> H <sup>+</sup> , NH <sub>2</sub> <sup>+</sup> , NH <sub>3</sub> <sup>+</sup> , NH <sub>4</sub> <sup>+</sup>
Surface species	N(s), H(s), NH(s), NH <sub>2</sub> (s), NH <sub>3</sub> (s) <sup>a</sup>
Electrons	e <sup>–</sup>

<sup>a</sup>This species only participates in the activation energy and entropy barrier calculations.

**Table 2. Ranges of Manipulable Process Parameters in the Microkinetic Model Coupled with DFT Calculations**

	$T$ (K)	$n_e$ (cm <sup>–3</sup> )	$E$ (V/Å)	N <sub>2</sub> (vol %)
Range	300–600	5 × 10 <sup>7</sup> to 5 × 10 <sup>9</sup>	5 × 10 <sup>–5</sup> to 12 × 10 <sup>–5</sup>	0–100

surface electric field  $E_{\text{sur}}$  is different from that of the gas phase; we assume  $E_{\text{sur}}$  is proportional to the magnitude of the electric field in the gas phase.

### Surface Reactions

We systematically account for the influence of varying surface electric field strengths, denoted by  $E_{\text{sur}}$ , in the rate coefficient expressions of L-H and E-R reactions. In the ensuing subsections, we first provide an overview of the original rate coefficient expressions. Subsequently, we elucidate how these expressions are adapted to account for variable  $E_{\text{sur}}$ .

**L-H Reactions.** The L-H reactions are listed in Table S1. Diffusion activation energy barriers  $E_d$  of the L-H reactions are considered constant.<sup>17,25,41</sup> The diffusion energy barrier is the barrier for migration of surface adsorbed species.  $E_d$  is set to 0.2 eV based on H atoms approaching other adsorbed species on the Fe surface. This is because other adsorbed species (N(s), NH(s), NH<sub>2</sub>(s)) have higher  $E_d$  values and are thus harder to migrate during reactions,<sup>41,55</sup> given the assumption of abundance of sites used in this work. As a consequence, adsorbed H should transport to the closest sites to react. On the other hand, activation energy barriers  $E_a$  can vary with the surface electric field  $E_{\text{sur}}$ . We use DFT to calculate  $E_a$  in relation to the variable strength of  $E_{\text{sur}}$ ; this is further detailed below. The expression for the rate coefficients of the L-H reactions takes the form of

$$k_{\text{LH}} = \frac{\nu}{4S_T} \exp\left(-\frac{E_d + E_a}{k_B T_w}\right) \quad (2)$$

where  $T_w$  is the surface temperature, which is assumed to be the same as the gas-phase temperature  $T$ ;  $\nu$  is the surface diffusional jump frequency, the value of which is set to 10<sup>13</sup> s<sup>–1</sup> according to refs 41 and 55 for metal surfaces;  $S_T$  is the total surface site density, set to 10<sup>15</sup> cm<sup>–2</sup> based on refs 41 and 56 and assumed to be abundant.  $k_B$  is the Boltzmann constant.

A common approach to calculate  $E_a$  is via transition-state theory in DFT using the nudged elastic band (NEB) method,<sup>57,58</sup> which relies on finding transition states. In thermal catalysis,  $E_a$  is commonly estimated using the Bell-Evans-Polanyi (BEP) principle.<sup>59–65</sup> For metal catalysts, BEP indicates the difference in activation energy between two reactions of the same family is proportional to the difference of their enthalpy of reaction.<sup>65</sup> That is,

$$E_a = E_0 + \alpha \Delta H \quad (3)$$

where  $\Delta H$  is the enthalpic change of the reaction;  $\alpha$  characterizes the position of the transition state along the reaction coordinate (such that 0 ≤  $\alpha$  ≤ 1), and  $E_0$  is the activation energy of a reference reaction. Che et al.<sup>66</sup> show that BEP correlation can be used for simple surface reactions such as C–H breaking and O–H formation. In plasma-catalytic NH<sub>3</sub>

synthesis, the main L-H surface reactions are the processes of N–H formation, for which we assume BEP correlation remains valid. The enthalpic change of a reaction is obtained by calculating the difference between the energies of reactants and products. For example,  $\Delta H$  for  $N(s) + H(s) \rightarrow NH(s) + (s)$  is

$$\Delta H = E_{NH(s)} + E_{(s)} - E_{H(s)} - E_{N(s)} \quad (4)$$

where the energies of reactants and products ( $E_{NH(s)}$ ,  $E_{(s)}$ ,  $E_{H(s)}$ ,  $E_{N(s)}$ ) are obtained by geometry optimization via DFT. BEP correlations for the three L-H reactions are taken from refs 27 and 67, as listed in Table S2.

**E-R Reactions.** In plasma catalysis studies,<sup>25,41,68</sup> the E-R reactions are commonly defined in terms of the sticking probability  $\gamma_{ER}$ , which describes the probability of a molecule being trapped on a surface. Accordingly, the rate coefficients for the E-R reactions are defined as

$$k_{ER} = (\tau_{ER} S_T)^{-1} = \left[ \frac{\Lambda^2}{D} + \frac{V}{A} \frac{2(2 - \gamma_{ER})}{\bar{v} \gamma_{ER}} \right]^{-1} S_T^{-1} \quad (5)$$

where  $\tau_{ER}$  is the decay time of a gas-phase species due to diffusion and adsorption losses on the surface;  $S_T$  is the total surface site density and is the same as in eq 2;  $\Lambda$  is the diffusion length, set as 0.1 mm, and  $\frac{V}{A}$  is the ratio of volume to area of the reactor. With the discharge volume  $V$  of 48.6 cm<sup>3</sup>, catalyst surface area of 3370 cm<sup>2</sup>, and a roughness factor of 2.1,  $\frac{V}{A}$  is 0.00687 cm.<sup>25</sup>  $\bar{v}$  is the thermal velocity of atoms and radicals.  $D$  is the diffusion coefficient. Under 300 K and 1 atm, the diffusion coefficient has a value of  $7.9 \times 10^{-5}$  m<sup>2</sup>s<sup>-1</sup>, denoted by  $\bar{D}$ . Under different temperatures and pressures,  $D$  can then be approximated as

$$\frac{D}{\bar{D}} = \frac{T^{3/2}}{300^{3/2}} \frac{1}{p} \quad (6)$$

where  $p$  is pressure with the unit of atm.<sup>25,69</sup>

Hays et al.<sup>70</sup> proposed a theoretical model for calculating  $\gamma$  based on the probability  $P_1$  of a gas atom recombining with a surface atom as it reaches the surface and the probability  $P_2$  of a gas atom reaching the surface after arriving at the pseudolayer. In this model, the activation energy and entropy barriers are considered because  $P_1$  is governed by the surface activation energy and  $P_2$  is influenced by entropic barriers that a molecule must overcome. Mortensen et al.<sup>71</sup> proposed the following expression for  $\gamma$  for metal surfaces

$$\gamma = \frac{1}{F \mathcal{A}} \frac{k_B T}{h} e^{\Delta S/k_B} e^{-E_a/k_B T} \quad (7)$$

where  $F = \bar{p} / \sqrt{2\pi m k_B T}$  is the flux of molecules hitting the surface;  $\bar{p}$  is the partial pressure of the reactant gas molecule;  $\mathcal{A}$  is the area per site that depends on surface geometry;  $k_B$  is Boltzmann constant;  $h$  is Planck's constant; and  $\Delta S$  is the entropy change. Additionally, Mortensen et al. suggested that the sticking probability  $\gamma$  could be dominated by either activation energy or entropic barriers.<sup>71</sup> For the E-R reactions considered in this work, however, it is assumed all the reactions that rely on the sticking probability are manipulated by entropic barriers.<sup>27,72</sup> The only special case is  $H_2 + NH(s) \rightarrow NH_3 + (s)$ , where the energy barrier of  $H_2$  dissociative adsorption dominates. Therefore, for this reaction, the reaction energy, instead of the entropy change, is used for computing  $\gamma_{ER}$ . A recent microkinetic model for plasma-catalytic ammonia synthesis also used entropic barriers to modify the Arrhenius-like E-R reaction rate coefficients.<sup>29</sup>

Here, we use the  $\gamma_{ER}$  values in Table S4 as the standard case  $\gamma_{std}$  to determine the corresponding standard entropy changes  $\Delta S_{std}$ .<sup>25</sup> Taking the ratio of  $\gamma_{ER}$  to  $\gamma_{std}$  and assuming ideal gas law, we have

$$\frac{\gamma_{ER}}{\gamma_{std}} = \begin{cases} \frac{\bar{p}_{std} T^{1.5} e^{\Delta S/k_B}}{\bar{p} T_{std}^{1.5} e^{\Delta S_{std}/k_B}} & \text{if dominated by entropic barrier} \\ = \frac{N_{std} T^{1.5} e^{\Delta S/k_B}}{N T_{std}^{1.5} e^{\Delta S_{std}/k_B}} \\ \frac{\bar{p}_{std} T^{1.5} e^{-\Delta H/k_B}}{\bar{p} T_{std}^{1.5} e^{-\Delta H_{std}/k_B}} & \text{if dominated by reaction barrier} \\ = \frac{N_{std} T^{1.5} e^{-\Delta H/k_B T}}{N T_{std}^{1.5} e^{-\Delta H_{std}/k_B T_{std}}} \end{cases} \quad (8)$$

where  $N$  is the total number of gas-phase reactant molecules and radicals. The standard case  $\gamma_{ER}$  is taken from ref 25 when the simulation conditions maximize the  $NH_3$  number density at the end of the process (3600 s). The chosen standard condition is  $N_2$  vol % = 33.33%,  $T = 400$  K,  $p = 1$  atm,  $E_r = 45.1$  Td, and  $n_e = 8.27 \times 10^7$  cm<sup>-3</sup>, under which the  $\gamma_{std}$  values for the E-R reactions are listed in Table S4. In eq 8,  $\Delta S$  is defined as the entropy difference between products and reactants. For instance,  $\Delta S$  of reaction  $N+H(s) \rightarrow NH(s)$  is

$$\Delta S = S_{NH(s)} - S_{H(s)} - S_N \quad (9)$$

where  $S_{NH(s)}$  and  $S_{H(s)}$  are the entropies of adsorbed NH and H on the surface, and  $S_N$  is the entropy of N radicals in the gas phase. Here, the entropy of surface is neglected assuming that the catalyst remains unchanged before and after adsorption, although the movement of surface atoms can impact adsorbate translations on the surface, thus influencing the entropy changes during adsorptions.<sup>73</sup> When a gas-phase molecule is adsorbed on the catalyst surface, the main loss of entropy arises from the translational freedom loss. Engelmann et al. calculated the entropy change  $\Delta S$  for each of the E-R reactions of ammonia synthesis by directly considering that the gas-phase reactants will lose all their entropy (or gain all their entropy from the gas-phase products), assuming surface adsorbed species do not have any entropy.<sup>29</sup> Alternatively, Campbell et al. observed that these adsorbed species on mineral and metal surfaces retain most of their gas-phase entropy.<sup>74</sup> They proposed the following empirical formula to correlate the entropy  $S_{ads}$  of the adsorbed state and the gas-phase entropy  $S_{gas}$

$$S_{ads} = 0.7 S_{gas} - 3.3 k_B \quad (10)$$

The above formula can serve as a general approximation for all mineral and metal surfaces, while the parameters 0.7 and 3.3 must be adjusted for a specific surface. Here, we use eq 10 to determine the entropy of the adsorbed state. To calculate the gas-phase entropy of molecules and radicals, the following equations are used to determine the entropic contributions from translation, rotation, and vibration

$$S(T) = S_{vib}(T) + S_{rot}(T) + S_{trans}(T) \quad (11a)$$

$$S_{trans} = k_B \ln \left[ \frac{V}{N} \left( \frac{2\pi m k_B T}{h^2} \right)^{3/2} \right] + \frac{5}{2} k_B \quad (11b)$$

$$S_{rot,linear} = k_B \ln \left( \frac{8\pi^2 I k_B T}{\sigma h^2} \right) + k_B \quad (11c)$$

$$S_{rot,nonlinear} = \frac{k_B}{2} \ln \left( \frac{\pi}{\sqrt{\sigma}} \frac{8\pi^2 c I_A}{h} \frac{8\pi^2 c I_B}{h} \frac{8\pi^2 c I_C}{h} \left( \frac{k_B T}{hc} \right)^3 \right) + \frac{3}{2} k_B \quad (11d)$$

$$S_{vib} = k_B \sum_i \frac{h\nu_i/k_B T \exp(-h\nu_i/k_B T)}{1 - \exp(-h\nu_i/k_B T)} - k_B \sum_i \ln[1 - \exp(-h\nu_i/k_B T)] \quad (11e)$$

where  $V$  is the discharge volume,  $N$  is the total number of molecules and radicals,  $\sigma$  is the symmetry number of a molecule or radical,  $c$  is the speed of light,  $\nu_i$  is the  $i^{\text{th}}$  mode of the vibrational frequency of a

molecule or radical, and  $I$  is the moment of inertia. For a nonlinear molecule or radical, the eigenvalues of the moment of inertia tensor  $I_A$ ,  $I_B$ , and  $I_C$  are used, since the moment of inertia should be calculated based on orthogonal Cartesian coordinates. The standard entropies  $S_{\text{std}}$  (including  $n_{\text{std}} = \frac{N_{\text{std}}}{V}$ ,  $S_{\text{trans}}$ ,  $S_{\text{rot}}$ , and  $S_{\text{vib}}$ ) of the gas-phase reactant molecules/radicals used for  $\Delta S_{\text{std}}$  calculations are listed in Table S5. The standard reaction energy  $\Delta H_{\text{std}}$  of  $\text{H}_2 + \text{NH}(\text{s}) \rightarrow \text{NH}_3 + (\text{s})$  is 1.04 eV. From DFT calculations, we observed that electric field  $E$  can influence entropic barriers by changing the number density of gas-phase species, moment of inertia  $I$ , and vibrational frequencies  $\nu_i$  of different modes. Based on the above discussion, the E-R reaction rate coefficients depend on temperature  $T$ , partial pressure  $\bar{p}$ , and electric field  $E$ . These coefficients change over time, since the number density of gas-phase species evolves over time.

**Recombination Reactions.** Only E-R reaction mechanisms are considered for the recombination reactions forming gas-phase  $\text{N}_2$  and  $\text{H}_2$ . This is because the diffusion activation energy barrier for diffusion of N atoms is too high.<sup>25,41,75</sup> Additionally,  $\text{H}_2$  formation from the L-H reaction of two adsorbed H atoms usually has a lower contribution in comparison with the E-R reaction.<sup>25,55,76</sup> The sticking probabilities of the two recombination reactions under standard conditions are listed in Table S6. The rate coefficient of the recombination reactions is calculated similarly to the above-described E-R reactions.

**Adsorption Reactions.** The direct adsorption reactions are listed in Table S7. Their sticking probability for direct adsorption of radicals to a clean metal surface is assumed to be 1, as in ref 77.

**Dissociative Adsorption Reactions.** Dissociative adsorption reactions can play an important role in plasma-catalytic ammonia synthesis. In particular, vibrationally excited  $\text{N}_2$  and  $\text{H}_2$  species can decrease the activation energy barrier, therefore leading to production of H(s) and especially N(s).<sup>77,68</sup> To this end, Mehta et al. proposed an Arrhenius-like rate coefficient expression for vibrationally excited  $\text{N}_2$  dissociative adsorption.<sup>17</sup> Alternatively, Hong et al. adopted an approximated parametrized expression for the sticking probability of vibrationally excited  $\text{N}_2$  dissociative adsorption,<sup>78–80</sup> which is the approach taken here.

### Density Functional Theory Calculations

Plane-wave DFT calculations are performed using Quantum ESPRESSO (QE) v.6.4.1 *ab initio* code<sup>81–83</sup> and the Python ASE package<sup>84</sup> for slab construction and analysis. The DFT calculations are performed using computational resources provided by the Advanced Cyberinfrastructure Coordination Ecosystem: Services & Support (ACCESS) program.<sup>85</sup> We use Purdue-Burke-Ernzerhof (PBE) exchange-correlation functional<sup>86</sup> with the standard solid-state pseudopotentials (SSSP)<sup>87</sup> and Grimme-D2 van der Waals corrections.<sup>88–90</sup> The energy cutoff of 60 Ry is set for wave functions, whereas the kinetic energy cutoff of 480 Ry is used for charge density and potential.<sup>91</sup> Spin polarization is enabled for all calculations. To accelerate energy convergence for the number of  $k$ -points, Methfessel-Paxton method<sup>92</sup> is used with a smearing parameter of 0.01. Convergence of electronic and atomic configurations is achieved when the energy and forces fall below  $10^{-5}$  eV and  $10^{-2}$  eV/Å, respectively.

Fe(110) slabs are created via ASE by cleaving bulk unit cells. The unit cell is obtained via “vc-relax” in QE, allowing the lattice constant to be optimized. The same setting as discussed above is used, except for employing  $12 \times 12 \times 12$  Gamma-centered  $k$ -point meshes, 90 Ry kinetic energy cutoff and 900 Ry energy cutoff. The resulting optimized lattice constant is 2.802 Å, which is consistent with PBE.<sup>93</sup> The Fe(110) slabs have a total of 4 layers, with  $4 \times 4$  Fe atoms for each layer. Periodicity in the  $z$  direction is disabled by using at least 20 Å vacuum between slabs in the direction perpendicular to the surface. Geometry optimizations for the slabs and adsorbate-slabs are performed using a  $4 \times 4 \times 1$   $k$ -point mesh while fixing the lower two layers of Fe(110) slabs. The relaxed structures of the Fe(110) slab with different adsorbates can be found in Figure S1. Increasing the mesh density did not show a significant change of adsorption energies. On the other hand, calculations on gas-phase isolated  $\text{N}_x\text{H}_y$  ( $x$  and  $y$  can be zero) are conducted under the gamma point with a  $20 \text{ \AA} \times 20 \text{ \AA} \times 20 \text{ \AA}$  orthogonal cell, where  $\text{N}_x\text{H}_y$  is in the center.

For DFT calculations under varying electric field strengths, we use Effective Screening Medium (ESM) method, which enables modeling charged surfaces under the existence of electric field/applied voltage.<sup>94,95</sup> This method leverages the Green’s function technique to modify the Poisson solver in the standard pseudopotential plane-wave scheme. It treats the slab sandwiched by semi-infinite medium, with vacuum in between. Unlike the alternative methods of saw-like potential and modern theory of polarization, the ESM method does not require dipole correction for polarized surfaces. Moreover, the saw-like method requires manual specification of suitable saw-like potential profiles for catalyst surfaces, and modern theory of polarization requires well-defined ground-state polarization that is not feasible for the metallic system considered in this work.<sup>94,96</sup> In addition, electric field near a surface (length scales of millimeter) is not necessarily the same as electric field on a surface (length scales of angstrom) where the adsorbed species exist. Moreover, the adsorbate can in turn influence the electric field. The use of the ESM method allows us to capture this phenomenon. Here, we refer to the surface electric field  $E_{\text{sur}}$  as the near surface (length scales of millimeter), which is used in QE to define the applied electric field used in the ESM method. As such, the real electric field that an adsorbed molecule experiences is not  $E_{\text{sur}}$ , but that inferred from the ESM method. Electric field is assumed to be directed at the Fe(110) surface since electrons are accumulated on the surface.  $E_{\text{sur}}$  is inferred from the electric field strength used in the microkinetic model by multiplying the average electric field in the reactor by an enhancement factor in the range of 1000 to 10000.<sup>25,97–100</sup>

To calculate the vibrational frequencies for entropy calculation, we only consider gas-phase molecules/radicals. The entropy of an adsorbed species is estimated using eq 10. However, the ESM method cannot be used to calculate vibrational frequencies due to its incompatibility with the Phonon package in QE. Therefore, we leveraged the saw-like method, which is commonly used for nonmetallic systems, and obtained the same relaxed system energies for gas-phase species as those obtained via the ESM method. The optimized wave function files are then used to obtain vibrational frequencies for entropy calculations.

### Global Sensitivity Analysis and Multiobjective Bayesian Optimization

Global sensitivity analysis using Sobol’ indices<sup>101,102</sup> is used to systematically investigate the contribution of each process parameter to process outputs of interest predicted by the microkinetic model coupled with DFT calculations. Sobol’ indices decompose variance of model outputs into summands of input parameters. This allows Sobol’ indices to quantify the contribution of each input parameter, as well as the interactions of the inputs, to the output variance.<sup>101,103</sup> We employ the Python library SALib<sup>104</sup> to perform the global sensitivity analysis. The outputs include species number densities and reaction rates. The calculation of Sobol’ indices for each output uses 5000 samples of the process parameters following a Sobol sequence.<sup>105</sup> The output for each sample is predicted at process time 4000 s.

To analyze how different process parameters impact the energy efficiency of  $\text{NH}_3$  synthesis, we consider the trade-off between rates of reactions that waste energy and the concentration of  $\text{NH}_3$  produced. The main reactions wasting energy are the  $\text{H}_2$  recombination (between H and H(s)) and  $\text{NH}_3$  decomposition (between  $\text{NH}_3$  and  $e^-$ ).<sup>25,40</sup> This is because H radicals are produced from collisions between  $\text{H}_2$  and high-energy electrons, thereby the reaction between H and H(s) forming  $\text{H}_2$  is detrimental to ammonia synthesis in ways of wasting energy and reducing available H and H(s) for  $\text{NH}_3$  synthesis.<sup>25,40</sup> Not only  $\text{NH}_3$  decomposition via collisions with electrons causes the loss of  $\text{NH}_3$ , it also wastes energy via reforming  $\text{NH}_3$ , which is equivalent to H exchanges.<sup>25,49,106</sup>

Investigating what combination of process parameters can maximize the number density of  $\text{NH}_3$  while slowing down the two processes resulting in energy loss is therefore essential. Note that the latter two objectives are conflicting. Here, we use multiobjective optimization<sup>42</sup> to construct the Pareto frontier to study the trade-off between these objectives. Since no closed-form expression exists for the number density of  $\text{NH}_3$  and the rates of the above reactions that lead to energy

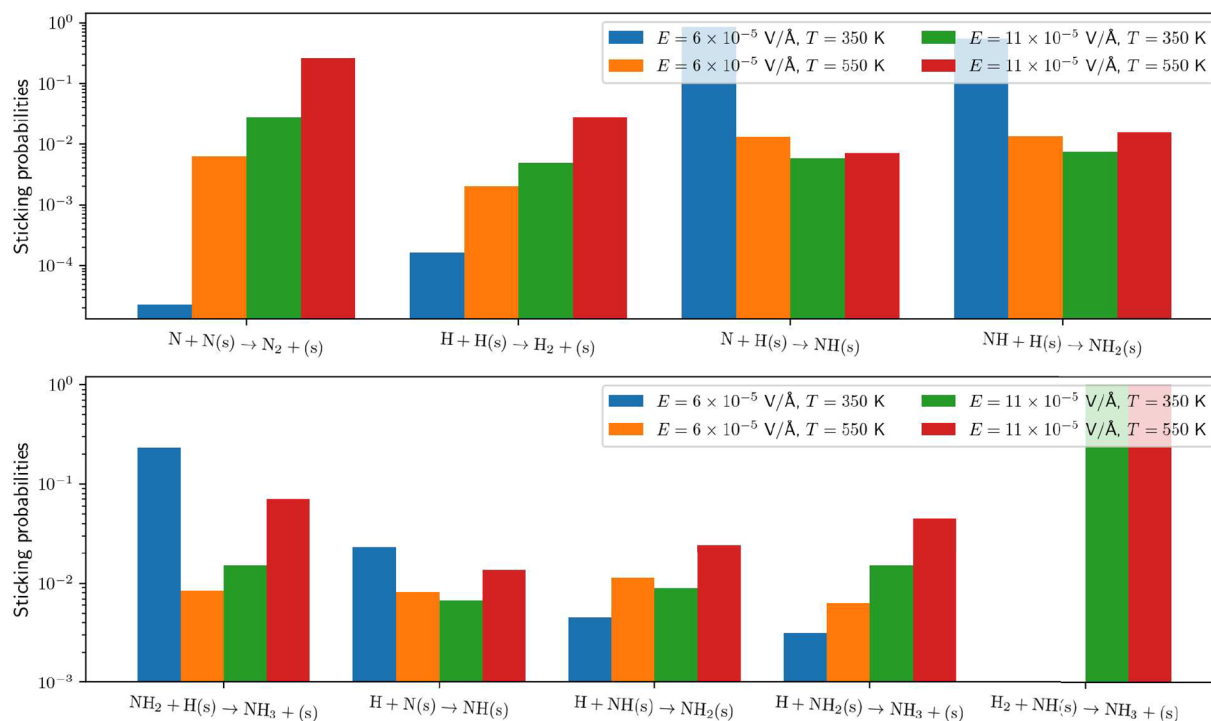


**Figure 3.** Sticking probabilities of E-R surface reactions for different combinations of electric field strength,  $E$ , and reactor temperature,  $T$ , under constant  $N_2$  vol % of 33% and electron number density of  $8.27 \times 10^5 \text{ cm}^{-3}$ .

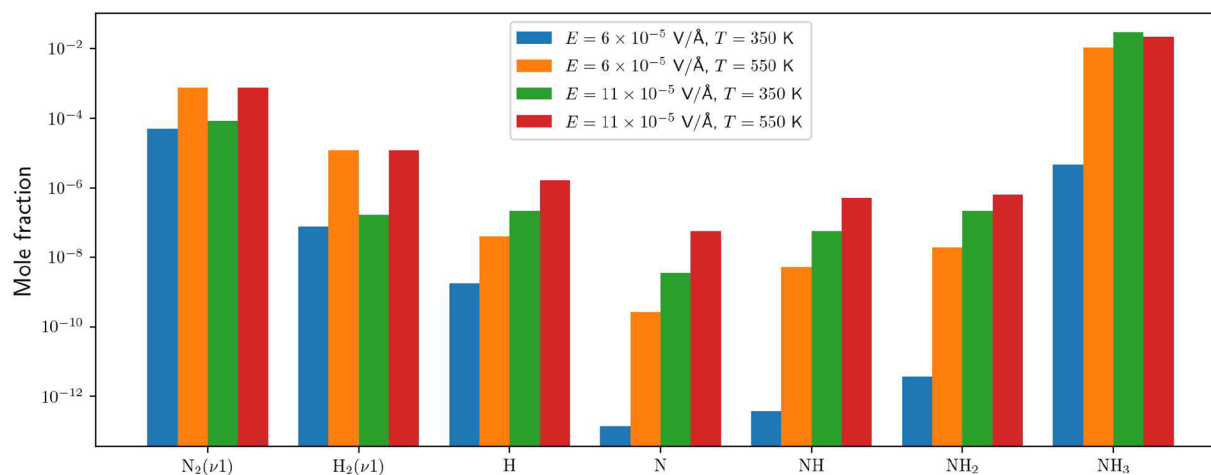


**Figure 4.** Mole fractions of gas-phase species critical to  $NH_3$  formation in relation to electric field strength,  $E$ , and temperature,  $T$ , under constant  $N_2$  vol % of 33% and electron number density of  $8.27 \times 10^5 \text{ cm}^{-3}$ .

loss, we formulate this problem as a multiobjective Bayesian optimization (MOBO) problem, which is especially useful for global optimization of black-box functions.<sup>43,107</sup> The Python library AX is utilized to solve the MOBO problem.<sup>108</sup> 10 random searches via Sobol' sequence are used to initialize the MOBO algorithm. We use radial basis function kernel<sup>109</sup> and the expected hypervolume improvement<sup>110</sup> acquisition function to, respectively, train a Gaussian process regression model for each objective and suggest the next query point for active learning of the process parameter space.

## RESULTS AND DISCUSSION

According to the rate expressions of the E-R reactions in eq 5 and L-H reactions in eq 2, the strength of electric field  $E$  and reactor temperature  $T$  should significantly impact surface reactions, thus influencing the  $NH_3$  reaction pathways. Therefore, we first examine the impact of  $E$  and  $T$  on surface reactions

as well as on the generation and loss of the main gas-phase and surface species. Subsequently, we perform a global sensitivity analysis to systematically study the contribution of each process parameter to the generation and loss of gas-phase and surface species, including  $NH_3$ . Finally, we use multiobjective Bayesian optimization to study the trade-offs between reaction rates that are responsible for energy dissipation and  $NH_3$  generation.

### Impact of Electric Field and Temperature

To study how  $E$  and  $T$  influence the surface reactions, important species, and reaction mechanisms, two levels (low and high) of  $E$  and  $T$  are chosen, forming a total of four combinations. The values of the two levels of  $E$  and  $T$  are  $\{6 \times 10^{-5} \text{ V/Å}, 11 \times 10^{-5} \text{ V/Å}\}$  and  $\{350 \text{ K}, 550 \text{ K}\}$ , respectively. The values of electron density  $n_e$  and  $N_2$  vol % are fixed at  $8.27 \times 10^7 \text{ cm}^{-3}$  and 33.33 vol %, respectively, which are selected according to ref 25 that

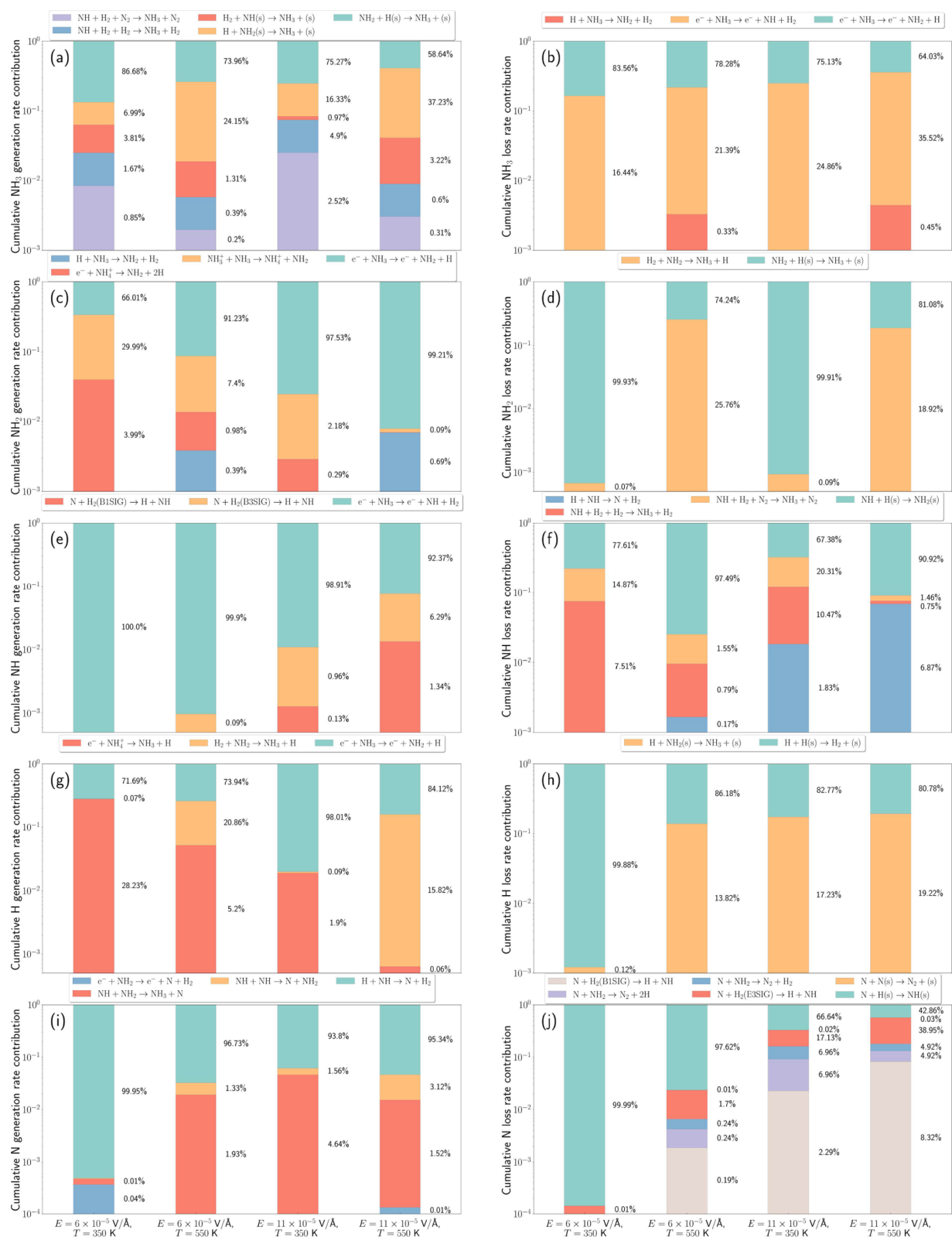


**Figure 5.** Contribution of dominant reactions producing and consuming  $\text{NH}_3$ ,  $\text{NH}_2$ ,  $\text{NH}$ ,  $\text{H}$ , and  $\text{N}$  with respect to different levels of electric field strength,  $E$ , and temperature,  $T$ , under constant  $\text{N}_2$  vol % of 33% and electron number density of  $8.27 \times 10^5 \text{ cm}^{-3}$ . (a, b) Contribution of reactions producing and consuming  $\text{NH}_3$ . (c, d) Contribution of reactions producing and consuming  $\text{NH}_2$ . (e, f) Contribution of reactions producing and consuming  $\text{NH}$ . (g, h) Contribution of reactions producing and consuming  $\text{H}$ . (i, j) Contribution of reactions producing and consuming  $\text{N}$ .

studied reaction mechanisms of plasma-catalytic  $\text{NH}_3$  synthesis under the “most favorable” process parameters via experiments and microkinetic modeling. The effects of  $n_e$  and  $\text{N}_2$  vol % are

studied in the next section. For each combination of the parameters, the reaction time is set to at least 4000 s to reach steady-state. Figure 3 demonstrates how the sticking proba-

bilities of the E-R reactions vary with respect to  $E$  and  $T$ . Note that the sticking probability of  $\text{H}_2 + \text{NH}(s) \rightarrow \text{NH}_3 + (s)$  is calculated according to its reaction energy instead of entropy due to the dominant energy barrier of dissociating  $\text{H}_2$ . As can be seen from Figure 3, the sticking probabilities of the E-R reactions may not monotonically change with  $E$  or  $T$ . This is due to the complex relation of the sticking probabilities to the partial pressure  $\bar{p}$  of the reactant gas-phase species and entropy changes  $\Delta S$  of species, which are nonlinearly affected by both  $T$  and  $E$ , as in eqs 7 and (8).

**Gas-Phase Species and Their Generation/Loss Mechanisms.** Figure 4 shows the mole fractions of gas-phase species  $\text{N}_2(\nu 1)$ ,  $\text{H}_2(\nu 1)$ , H, N, NH,  $\text{NH}_2$ , and  $\text{NH}_3$  under the four combinations of  $E$  and  $T$  at time 4000 s. These gas-phase species appear in the series of reactions forming  $\text{NH}_3$ . Their mole fractions vary as a function of both  $T$  and  $E$ ; increasing  $E$  and  $T$  results in a higher mole fraction for H, N, NH, and  $\text{NH}_2$  species. In contrast, the mole fractions of  $\text{N}_2(\nu 1)$  and  $\text{H}_2(\nu 1)$  only experience a slight increase when  $E$  increases. These changes in species mole fractions can directly influence the sticking probabilities of their corresponding E-R reactions, which serve as a conduit for the influence of  $E$  and  $T$  on the surface reactions. Although the observed trends are expected, it is interesting to note that  $\text{NH}_3$  mole fraction exhibits a slight decrease under high  $E$  and  $T$ . Hence, increasing  $E$  and  $T$  may not result in a higher concentration of  $\text{NH}_3$ , which can be attributed to the more pronounced decomposition of  $\text{NH}_3$  under high  $E$  and  $T$ . On the other hand, lower levels of both  $E$  and  $T$  yield a relatively lower  $\text{NH}_3$  mole fraction. Note that the mole fractions of  $\text{N}_2$  and  $\text{H}_2$  are not shown in Figure 4, as they are almost unchanged due to their large initial values.  $\text{H}_2(\nu 1)$  and  $\text{N}_2(\nu 1)$  mole fractions are shown here since it has been postulated that they facilitate dissociative adsorptions of vibrationally excited  $\text{H}_2$  and  $\text{N}_2$ .<sup>25,111,112</sup> Higher vibrational states of  $\text{H}_2$  and  $\text{N}_2$  are excluded as their contribution to  $\text{NH}_3$  formation is limited due to their low concentrations. Furthermore, this study finds minimal contribution from  $\text{H}_2(\nu 1)$  dissociative adsorption forming H(s), as shown in Figure 7(a), due to low population of  $\text{H}_2(\nu 1)$ .<sup>25,113</sup> Similar observations are made for  $\text{N}_2(\nu 1)$ , which can be attributed to its limited excitability.

Starting from the generation and loss mechanisms of  $\text{NH}_3$ , we trace the gas-phase species that play a key role in  $\text{NH}_3$  formation. Figure 5 depicts the contribution of important reactions producing and consuming  $\text{NH}_3$  and the corresponding important gas species, including H, N, NH,  $\text{NH}_2$ , at 4000 s for the four combinations of  $E$  and  $T$ . A reaction is considered to be dominant if it exhibits a notable reaction rate (i.e., the fastest reaction), or the reaction rate is within 10% of that of the fastest reaction) under any of these four combinations of  $E$  and  $T$ . The L-H reaction  $\text{NH}_2(s) + \text{H}(s) \rightarrow \text{NH}_3 + 2(s)$  is not depicted in Figure 5(a) due to its relatively lower significance compared to other reactions, primarily attributed to its high activation energy as determined by DFT calculations. Consequently, the important surface reactions responsible for  $\text{NH}_3$  production in Figure 5(a) originate exclusively from E-R reactions, where shifts in the  $\text{NH}_3$  surface reaction mechanisms can be observed due to their variable response to  $E$  and  $T$ . As compared to the dominant E-R surface reactions, the gas-phase reactions  $\text{NH} + \text{H}_2 + \text{H}_2 \rightarrow \text{NH}_3 + \text{H}_2$  and  $\text{NH} + \text{H}_2 + \text{N}_2 \rightarrow \text{NH}_3 + \text{N}_2$  have a smaller contribution to  $\text{NH}_3$  generation. In fact, variations in entropy changes of the gas-phase species H,  $\text{H}_2$ , NH,  $\text{NH}_2$ , and  $\text{NH}_3$  as a function of  $E$  and  $T$  play a key role on the extent to which the rate of E-R reactions change. This discrepancy in

entropy changes among species implies that the changes in sticking probabilities for different E-R reactions can differ substantially. This is because the sticking probabilities of different E-R reactions can vary substantially in relation to the entropy changes of the gas-phase species, as discussed above (see Figure 3). The generation of these H, N, NH, and  $\text{NH}_2$  is exclusively driven by the gas-phase reactions; see Figure 5(c,e,g,i). The desorption processes of these radicals from the catalyst surface are not considered in this work due to the assumption of abundant catalyst sites and the strong adsorption of radicals onto the catalyst surface. As a result, the desorption of H, NH, and  $\text{NH}_2$  radicals is considered negligible.

The main reactions of  $e^- + \text{NH}_3 \rightarrow e^- + \text{NH} + \text{H}_2$  and  $e^- + \text{NH}_3 \rightarrow e^- + \text{NH}_2 + \text{H}$  producing NH and  $\text{NH}_2$  are the decomposition processes of  $\text{NH}_3$ , as shown in Figure 5(b). As  $\text{NH}_3$  dissociative adsorption is not accounted for in the reactions, the loss of  $\text{NH}_3$  primarily stems from electron impacts with  $\text{NH}_3$ , closely resembling the model by Hong et al.<sup>25</sup> The  $\text{NH}_3$  decomposition reactions in Figure 5(b) are in fact a source of energy dissipation controlled by the electron number density. On the other hand, NH can also be produced from N reacting with excited  $\text{H}_2$  ( $\text{H}_2(\text{B3SIG})$  and  $\text{H}_2(\text{B1SIG})$ ) in Figure 5(e). However, the concentration of N radicals in the gas phase is usually low since the production of N in the gas phase via (excited)  $\text{N}_2$  dissociation is usually slow in comparison with  $\text{N}_2$  dissociative adsorption. Therefore, NH generation from the reaction between N and  $\text{H}_2$  is limited. This suggests that catalysts can play an important role in  $\text{NH}_3$  plasma-catalytic synthesis,<sup>17,25,27</sup> since the triple bonds of  $\text{N}_2$  are too stable to make  $\text{N}_2$  reactive. The loss of NH and  $\text{NH}_2$  mainly arises from the E-R surface reactions between these species and H(s), as in Figure 5(d,f). The reaction  $\text{NH}_2 + \text{H}(s) \rightarrow \text{NH}_3 + (s)$  is a primary source of forming  $\text{NH}_3$  (see Figure 5(a)). The loss of NH via  $\text{NH} + \text{H}(s) \rightarrow \text{NH}_2(s)$  is one of the main pathways leading to  $\text{NH}_3$  production. It is worth noting that the rates of E-R reactions all increase with higher values of  $E$  and  $T$ . However, as shown in Figure 3, the sticking probability does not necessarily increase with higher  $E$  and  $T$  for certain E-R surface reactions, including  $\text{N} + \text{H}(s) \rightarrow \text{NH}(s)$ ,  $\text{NH} + \text{H}(s) \rightarrow \text{NH}_2(s)$ , and  $\text{NH}_2 + \text{H}(s) \rightarrow \text{NH}_3 + (s)$ . For these reactions, the rate coefficients decrease due to the decrease in sticking probabilities. Hence, the increase in the reaction rates is attributed to the higher concentration of reactants under higher values of  $E$  or  $T$ .

We also consider the generation and loss of N atoms in the gas phase. As shown in Figure 5(j), under higher values of  $E$  or  $T$ , although the  $\text{NH}_3$  production is higher, the recombination process of  $\text{N} + \text{N}(s) \rightarrow \text{N}_2 + (s)$  will become faster, leading to more energy dissipation. However, compared to the recombination process of  $\text{H} + \text{H}(s) \rightarrow \text{H}_2 + (s)$  in Figure 5(h), the reformation of  $\text{N}_2$  via the E-R surface reaction is much less important (see Figure 5(j)). Additionally, the recombination reaction of  $\text{H}_2$  formation becomes faster as  $T$  and/or  $E$  increase. In fact, energy dissipation via the  $\text{H}_2$  recombination reaction has been shown to be important and should be minimized to enhance the energy efficiency of plasma-catalytic  $\text{NH}_3$  synthesis.<sup>25,114</sup> Yet, suppressing the  $\text{H}_2$  recombination reaction can conflict with maximizing  $\text{NH}_3$  production. Lowering  $E$  and/or  $T$  alone as a means of reducing the reformation rate of  $\text{H}_2$  can result in a decrease in the number density of  $\text{NH}_3$ .

In addition to the above reactions, we also study the reactions that yield "source" H and N atoms, which do not originate from the decomposition of critical species, namely,  $\text{NH}_3$ ,  $\text{NH}_2$ , and

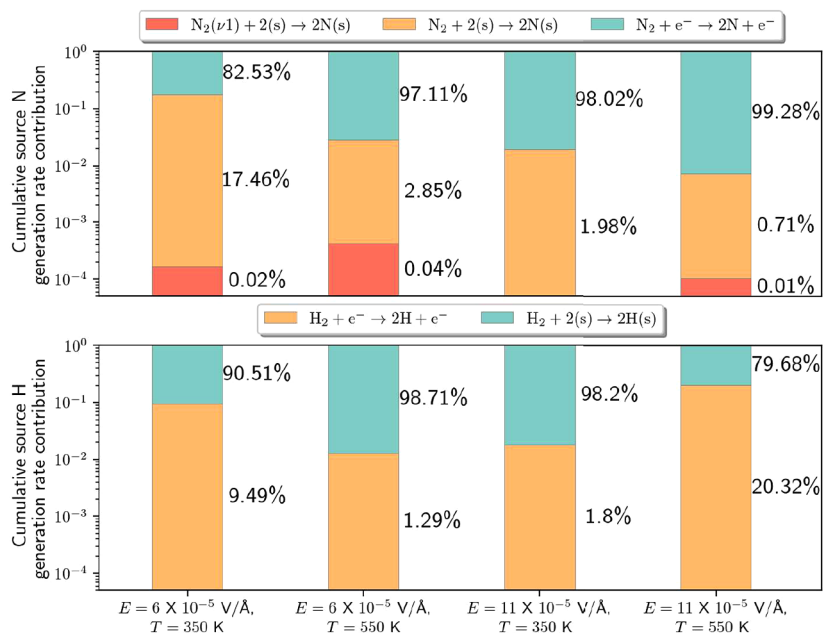


**Figure 6.** Contribution of dominant reactions producing “source” N and H atoms with respect to different levels of electric field strength,  $E$ , and temperature,  $T$ , under constant  $N_2$  vol % of 33% and electron number density of  $8.27 \times 10^5 \text{ cm}^{-3}$ . Top: Contribution of reactions producing “source” N atoms. Bottom: Contribution of reactions producing “source” H atoms.

NH. As shown in Figure 5(g,i), the majority of H and N production can be attributed to the breakdown of critical species. However, these reactions do not account for the generation of “source” N and H atoms; instead, they result in the creation of unproductive reaction cycles by consuming valuable species like  $NH_3$ . On the contrary, Figure 6 illustrates the generation of “source” N and H atoms, including adsorbed N and H. The reactions presented in Figure 6 exhibit notable reaction rates and are considered essential for producing “source” N and H.<sup>17,25,112,115</sup> As for “source” N production, the dominant reaction is the dissociation of  $N_2$  through electron collisions, while  $N_2$  dissociative adsorption prevails only under conditions of low gas temperature and low electric field strength. This observation is consistent with findings reported in the literature, where the enhanced  $N_2$  dissociative adsorption is suggested to result from vibrational excitation  $N_2(\nu)$ , lowering the energy barrier;<sup>17,112,115</sup> this observation is not attributed to a strong local electric field. Hence, given that the DFT-microkinetic model exclusively considers electric field effects, a decrease in the contribution of  $N_2$  dissociative adsorption to “source” N generation is expected as  $T$  and  $E$  increase, since higher temperatures promote gas-phase  $N_2$  dissociation.

As for the reactions contributing to “source” H generation, the dominant process is the dissociative adsorption of  $H_2$ . This is primarily because  $H_2$  dissociative adsorption tends to occur readily. Notably, gas-phase  $H_2$  dissociation via electron collisions only becomes significant under conditions of either low temperature and electric field strength or high temperature and electric field strength. This suggests that the influence of gas temperature and electric field strength on  $H_2$  dissociation via electron collisions is synergistic.

**Important Surface Species and Their Generation/Loss Mechanisms.** The microkinetic model takes into account only four adsorbed surface species, namely, H(s), N(s), NH(s), and  $NH_2(s)$ .  $NH_3(s)$  is not included in the microkinetic model, but its contribution is accounted for in the DFT calculations of activation energies and entropy changes for the L-H and E-R

reactions involving  $NH_3(s)$ . Table 3 lists the coverage fraction for the four surface species under the four combinations of  $E$  and

**Table 3. Coverage Fraction<sup>a</sup> of Adsorbed Surface Species with Respect to Different Levels of Electric Field Strength,  $E$ , and Temperature,  $T$ , under Constant  $N_2$  vol% of 33% and Electron Number Density of  $8.27 \times 10^5 \text{ cm}^{-3}$**

	$E = 6 \times 10^{-5}$ V/Å, $T = 350$ K	$E = 6 \times 10^{-5}$ V/Å, $T = 550$ K	$E = 11 \times 10^{-5}$ V/Å, $T = 350$ K	$E = 11 \times 10^{-5}$ V/Å, $T = 550$ K
H(s)	$9.85 \times 10^{-1}$	$8.86 \times 10^{-1}$	$8.31 \times 10^{-1}$	$7.97 \times 10^{-1}$
N(s)	$1.76 \times 10^{-5}$	$1.45 \times 10^{-4}$	$2.15 \times 10^{-4}$	$2.80 \times 10^{-4}$
NH(s)	$1.22 \times 10^{-6}$	$3.92 \times 10^{-8}$	$2.88 \times 10^{-9}$	$3.98 \times 10^{-8}$
$NH_2(s)$	$2.22 \times 10^{-4}$	$9.93 \times 10^{-2}$	$1.53 \times 10^{-1}$	$1.86 \times 10^{-1}$

<sup>a</sup>Note: The sum of the four coverage fractions may not equal to 1 since there could be free sites.

$T$ , assuming abundance of available surface sites.<sup>25,41</sup> Except for H(s), the other three species undergo large variations in their surface coverage. The considerably lower coverage fraction of NH(s) suggests that it may act as a bottleneck species, as it is rapidly consumed upon formation. This finding is consistent with observations in ref 116, where the downstream reaction pathway from NH(s) to  $NH_3$  is limited by the E-R formation of NH(s).

Figure 7 shows the contribution of generation and loss reactions for H(s), N(s), NH(s), and  $NH_2(s)$  under the four combinations of  $E$  and  $T$ . The large surface coverage of H(s) results from the strong dissociative adsorption  $H_2 + 2(s) \rightarrow 2H(s)$  on the catalyst surface, as shown in Figure 7(a), which also leads to the strong recombination process of  $H_2$  in Figure 7(b), causing a large energy dissipation.<sup>25,114</sup> The reformed  $H_2$  then consumes energy via the reaction  $H_2 + 2(s) \rightarrow 2H(s)$ , leading to generation of H(s). Other mechanisms of consuming H(s) include the E-R surface reactions with  $NH_2$ , NH, and N. As  $E$  and/or  $T$  increase, these E-R surface reactions become more dominant, while the recombination process becomes less

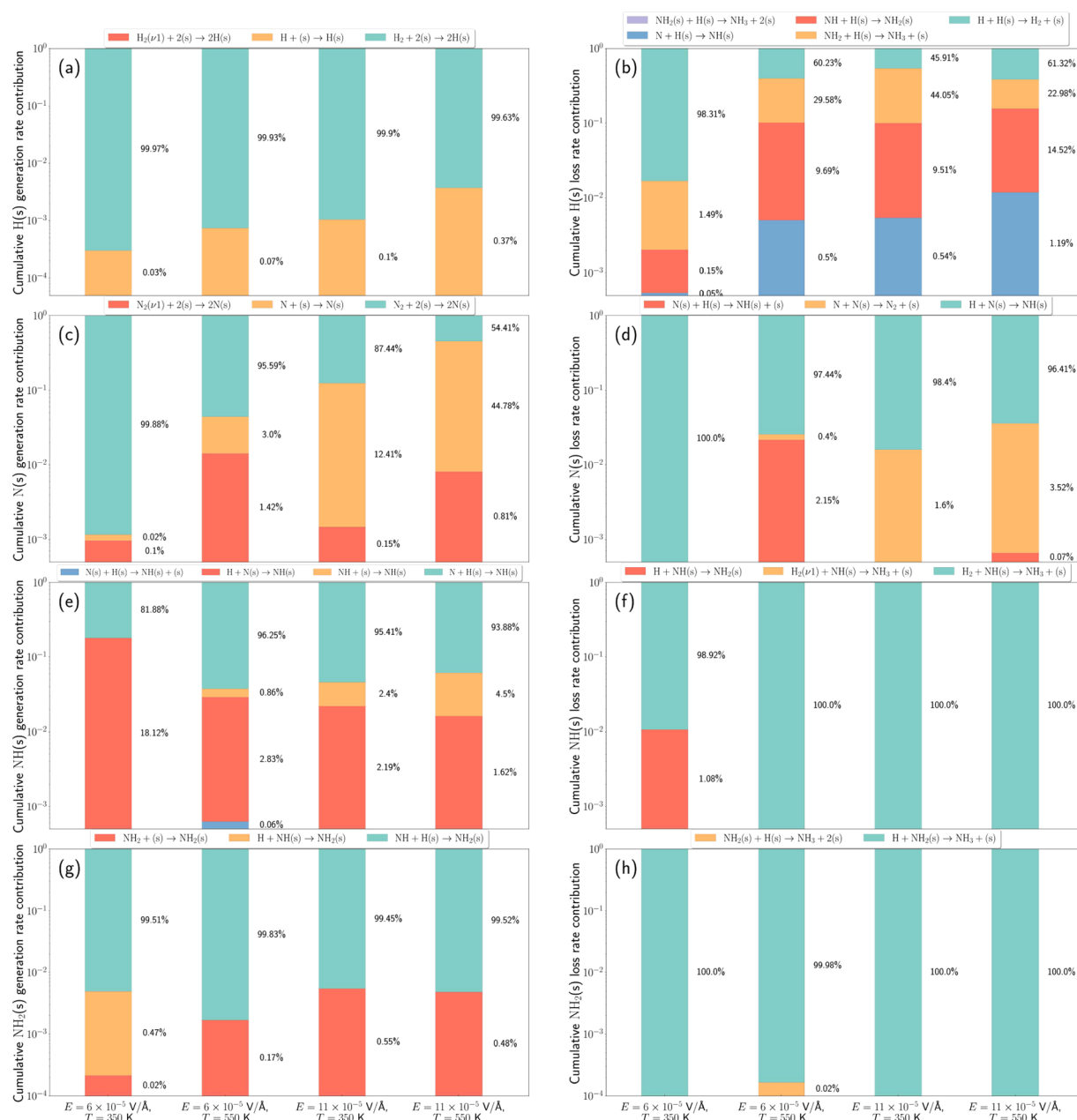


**Figure 7.** Contribution of dominant reactions producing and consuming H(s), N(s), NH(s), and NH<sub>2</sub>(s) with respect to different levels of electric field strength,  $E$ , and temperature,  $T$ , under constant N<sub>2</sub> vol % of 33% and electron number density of  $8.27 \times 10^5 \text{ cm}^{-3}$ . (a, b) Contribution of reactions producing and consuming H(s). (c, d) Contribution of reactions producing and consuming N(s). (e, f) Contribution of reactions producing and consuming NH(s). (g, h) Contribution of reactions producing and consuming NH<sub>2</sub>(s).

competitive with the exception under both high  $E$  and  $T$  where the recombination process becomes more competitive again. The largest change of reaction rates in relation to increased  $E$  and  $T$  (especially  $T$ ) occurs for the L-H surface reactions  $\text{NH}_2 + \text{H}(s) \rightarrow \text{NH}_3 + 2(s)$  and  $\text{N}(s) + \text{H}(s) \rightarrow \text{NH}(s) + (s)$ , although their contribution is almost negligible compared to other reactions in Figure 7(b,d). This is expected since the activation energy barriers of the L-H reactions calculated via DFT are higher than the values used in refs 9 and 25 due to the electric field effects considered in this study (see Tables S2 and S3). Although the activation energies decrease when increasing the electric field strength, their values are still too large to induce a significant increase in the reaction rate coefficients. This is while

temperature has a larger impact on the L-H reaction rates (see eq 2).

The formation of N(s) is mainly due to the dissociative adsorption of N<sub>2</sub> and the direct adsorption of N, as shown in Figure 7(c). At lower levels of  $E$  and  $T$ , the main source of N(s) generation is the dissociative adsorption reaction  $\text{N}_2 + 2(s) \rightarrow 2\text{N}(s)$ . However, as  $E$  and  $T$  increase, the direct adsorption reaction  $\text{N} + (s) \rightarrow \text{N}(s)$  becomes more competitive, particularly since N<sub>2</sub> is more prone to dissociation at higher  $T$  and  $E$ . The loss of N(s) is dominated by the E-R reaction of  $\text{H} + \text{N}(s) \rightarrow \text{NH}(s)$ . The recombination reaction forming N<sub>2</sub> will become more significant with increasing  $E$  and/or  $T$ . Again,  $T$  has a significant impact on the L-H reaction  $\text{N}(s) + \text{H}(s) \rightarrow$

NH(s) + (s), which consumes N(s), due to its large activation energy barrier (see Figure 7(d)).

Notable changes in the contribution of NH(s) generation reactions are observed in Figure 7(e), indicating that the reaction pathways governing NH(s) and even NH<sub>3</sub> formation can vary nonlinearly in relation to *E* and *T*. As shown in Figure 7(f), the generated NH(s) is almost entirely consumed by H<sub>2</sub>+NH(s) → NH<sub>3</sub>+ (s), which is one of the sources producing NH<sub>3</sub>. Lastly, the generation and consumption mechanisms of NH<sub>2</sub>(s) are mainly governed by NH + H(s) → NH<sub>2</sub>(s) and H + NH<sub>2</sub>(s) → NH<sub>3</sub>(s), respectively; see Figure 7(g,h).

**Summary of Changes in Gas-Phase and Surface Reactions under Varying *E* and *T*.** It follows from the above that even under constant N<sub>2</sub> vol % and electron number density, variations in the rates of different gas-phase and surface reactions are nonlinear and highly correlated with each other under varying electric field strength and gas temperature. This is due to the sticking probabilities of the E-R surface reactions that are influenced by the entropies of the related species. Table 4

**Table 4. Summary of Changes in the Gas-Phase and Surface Reactions in Plasma-Catalytic Synthesis of NH<sub>3</sub> in Relation to Varying Levels of Electric Field Strength, *E*, and Temperature, *T*, under Constant N<sub>2</sub> vol% of 33% and Electron Number Density of 8.27 × 10<sup>5</sup> cm<sup>-3a</sup>**

Reaction	Low <i>E</i> , low <i>T</i>	Low <i>E</i> , high <i>T</i>	High <i>E</i> , low <i>T</i>	High <i>E</i> , high <i>T</i>
Generation of "source" N				
N <sub>2</sub> +e <sup>-</sup> → 2N+e <sup>-</sup>	★	★	★	★
N <sub>2</sub> +2(s) → 2N(s)	★	☆	☆	
Generation of "source" H				
H <sub>2</sub> +e <sup>-</sup> → 2H+e <sup>-</sup>	★	☆	☆	★
H <sub>2</sub> +2(s) → 2H(s)	★	★	★	★
Generation of N(s)				
N <sub>2</sub> +2(s) → 2N(s)	★	★	★	★
N+(s) → N(s)		☆	★	★
Loss of N				
N+H(s) → NH(s)	★	★	★	★
N+H <sub>2</sub> (s) → H+NH			★	★
Generation of NH(s)				
N+H(s) → NH(s)	★	★	★	★
H+N(s) → NH(s)	★	☆	☆	☆
NH+(s) → NH(s)		☆	☆	☆
N(s)+H(s) → NH(s)+(s)		☆		
Generation of NH <sub>2</sub> (s)				
NH+H(s) → NH <sub>2</sub> (s)	★	★	★	★
Generation of NH <sub>3</sub>				
H+NH <sub>2</sub> (s) → NH <sub>3</sub> + (s)	☆	★	★	★
NH <sub>2</sub> +H(s) → NH <sub>3</sub> + (s)	★	★	★	★
H <sub>2</sub> +NH(s) → NH <sub>3</sub> + (s)	☆			☆
Loss of NH <sub>3</sub>				
e <sup>-</sup> +NH <sub>3</sub> → e <sup>-</sup> +NH <sub>2</sub> +H	★	★	★	★
e <sup>-</sup> +NH <sub>3</sub> → e <sup>-</sup> +NH+H <sub>2</sub>	★	★	★	★

<sup>a</sup>Blank: unimportant reactions. ☆: less dominant reactions. ★: dominant reactions.

presents the main gas-phase and surface reactions that take part in the plasma-catalytic NH<sub>3</sub> synthesis and how their importance changes with variations in *E* and *T*. The changes in the reaction mechanisms are illustrated in Figure 8. In particular, the dominance of some of the surface reactions changes under varying levels of *E* and *T*. For instance, under high *E* and *T*, N + (s) → N(s) exhibits a contribution nearly equal to that of N<sub>2</sub> + 2(s) → 2N(s), where N(s) is the main nitrogen source for plasma-catalytic NH<sub>3</sub> synthesis. This behavior arises due to the enhanced dissociation of N<sub>2</sub> in the gas phase caused by the higher *T* and *E*. On the other hand, under high *E* and/or *T*, N + H(s) → NH(s) assumes dominance, while its contribution is comparable to that of H + N(s) → NH(s) under low *E* and *T*. This observation is consistent with similar findings reported in refs 39, 116, and 117 as H(s) is generally abundant under different levels of *T* and *E*, making N + H(s) → NH(s) more favorable compared to H + N(s) → NH(s). Additionally, Table 4 does not include any L-H surface reactions except for N(s) + H(s) → NH(s) + (s). This finding is consistent with the previous observations,<sup>29,116</sup> which indicate that L-H reactions play a less significant role in plasma catalysis on non-noble catalysts compared to E-R surface reactions. The role of N(s) + H(s) → NH(s) + (s) becomes more dominant specifically under low *E* but high *T*. For the formation of NH<sub>3</sub>, the E-R reaction of NH<sub>2</sub> + H(s) → NH<sub>3</sub> + (s) has been reported to be important.<sup>25</sup> However, our findings suggest that the E-R reaction of H + NH<sub>2</sub>(s) → NH<sub>3</sub> + (s) will become equivalently dominant under high *T* and *E*. Recently, Zhe<sup>118</sup> has reported the significance of H + NH<sub>2</sub>(s) → NH<sub>3</sub> + (s), where disabling this reaction leads to a notable decrease in NH<sub>3</sub> yield. We conjecture that the increased coverage of NH<sub>2</sub>(s), as demonstrated in Table 3, could partly contribute to the importance of this reaction under high *T* and *E*. Furthermore, as illustrated in Figure 3, *T* exerts a greater influence on the sticking probability of NH<sub>2</sub> + H(s) → NH<sub>3</sub> + (s), as compared to H + NH<sub>2</sub>(s) → NH<sub>3</sub> + (s).

#### Global Sensitivity Analysis of Gas-Phase and Surface Reactions and Amount of NH<sub>3</sub> Produced

A global sensitivity analysis is performed to further investigate the effects of the four process parameters, namely, the inlet N<sub>2</sub> vol %, electron number density *n<sub>e</sub>*, electric field strength *E*, and temperature *T*, on the quantities of interest. We considered two cases: 1. the microkinetic model with the modified E-R and L-H reaction rate expressions informed by DFT calculations (termed as DFT-microkinetic model); and 2. the original microkinetic model from ref 25 that does not account for the effects of electric field on the surface reactions (termed as microkinetic model). For each of these models and each quantity of interest, 5000 different combinations of process parameters in the hypercube defined in Table 2 are used to calculate the total Sobol' index for each process parameter. The quantities of interest include the number density of gas-phase and surface species at steady-state, as well as the gas-phase and surface reaction rates. The total Sobol' index of a parameter indicates the overall contribution of the parameter to the variance of a quantity of interest.

We first compute the total Sobol' indices, *S<sub>T,NH<sub>3</sub></sub>*, for the NH<sub>3</sub> number density at steady-state with respect to the four process parameters, as shown in Figure 9. The Sobol' indices for the number density of NH<sub>3</sub> show a significant difference between the two models. In the microkinetic model, N<sub>2</sub> vol % has a much larger Sobol' index, followed by temperature *T*, electron number density *n<sub>e</sub>*, and electric field strength *E*, as shown in Figure 9. Yet, these results reveal that the predictions of the original

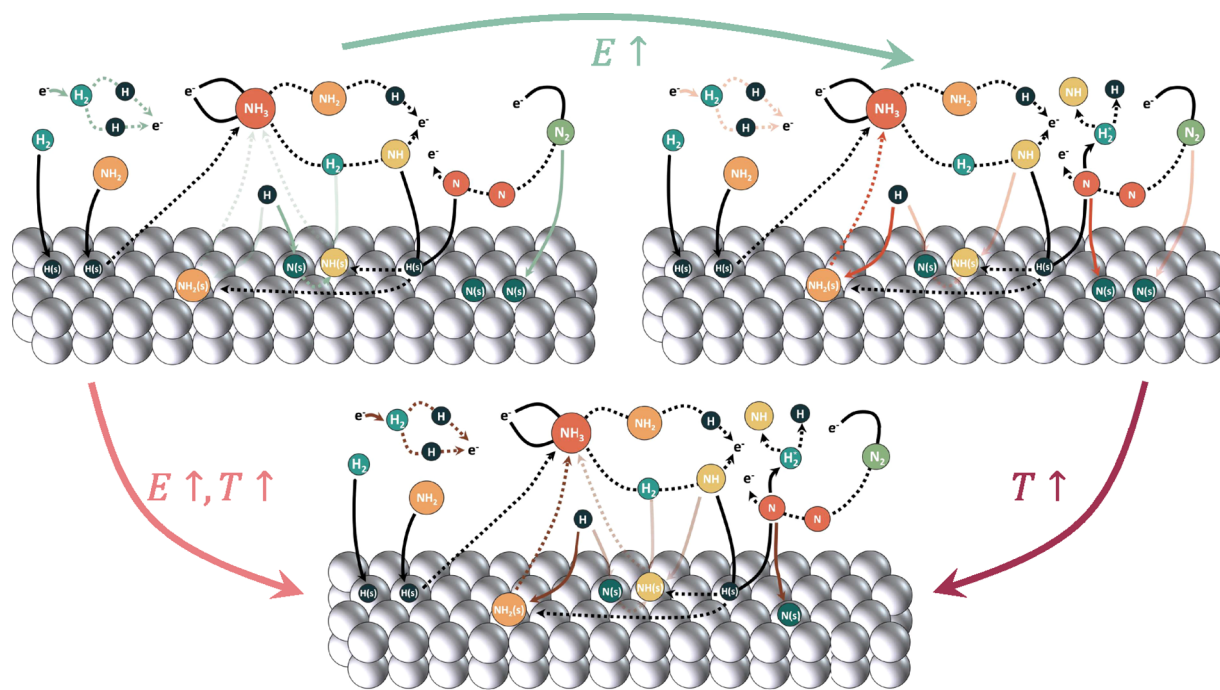


**Figure 8.** Illustration of how the gas-phase and surface reactions in the plasma-catalytic ammonia synthesis change in relation to changes in the electric field strength  $E$  and gas/surface temperature  $T$ . For a given combination of  $E$  and  $T$ , the dominant reactions are depicted with opaque arrows, while the less-dominant reactions are shown with fainter, translucent arrows. For each reaction, solid lines/arrows signify reactants, while dashed lines/arrows indicate products.

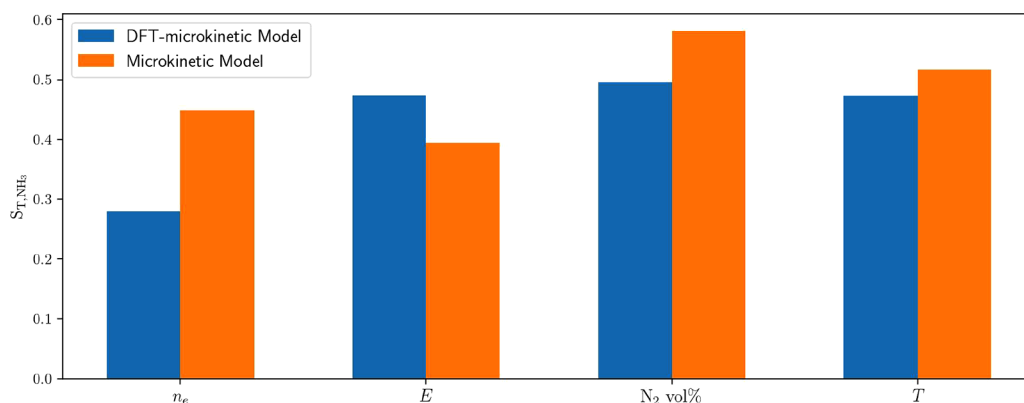


**Figure 9.** Global sensitivity analysis of  $NH_3$  number density at 4000 s with respect to the four process parameters using the microkinetic model and the microkinetic model coupled with DFT calculations that describe the effects of electric field on surface reactions.  $S_{T,NH_3}$  denotes the total Sobol' indices of  $NH_3$  number density approximated using 5000 samples.

microkinetic model that disregards the effects of electric field may not be fully consistent with experimental evidence. For example, refs 18, 119, and 120 have shown that, within the range of 300 to 600 K, the impact of  $T$  on  $NH_3$  concentration under low inlet gas flow rates is either equivalent or lower than that of the electric field  $E$ . Another major parameter is the energy input to the reactor, which is paramount for the electric field effects considered in this work. This is because the energy input dictates the electron temperature, which is calculated from reduced electric field by assuming Maxwellian distribution via BOLSIG+.<sup>47</sup> Therefore, it may not be justifiable that the effect of  $N_2$  vol % on  $NH_3$  production is much more significant than  $T$  and  $E$ . In contrast, as illustrated in Figure 9, the DFT-microkinetic model demonstrates a decrease in the importance of  $N_2$  vol %, while the significance of electric field is higher relative to the case of the microkinetic model. Moreover, the importance of  $T$  and  $E$  is

comparable in the DFT-microkinetic model, which predicts a reduced contribution of temperature to  $NH_3$  production while the contribution of electric field is increased. The decrease in the importance of temperature is expected, considering that catalyst effects on  $NH_3$  production should be negligible between 25 to 175 °C,<sup>18</sup> which covers about half of the examined temperature range in this work. Nonetheless, as compared to experimental observations,<sup>18</sup> a more pronounced reduction in the contribution of temperature would have been expected. This discrepancy between predictions of the DFT-microkinetic model and experimental observations can be due to unaccounted plasma-catalyst interactions, such as surface charge effects, in the DFT calculations. Despite this, the DFT-microkinetic model predictions match experimental observations more closely than the predictions of the microkinetic model. It is however challenging to describe the importance of electron number

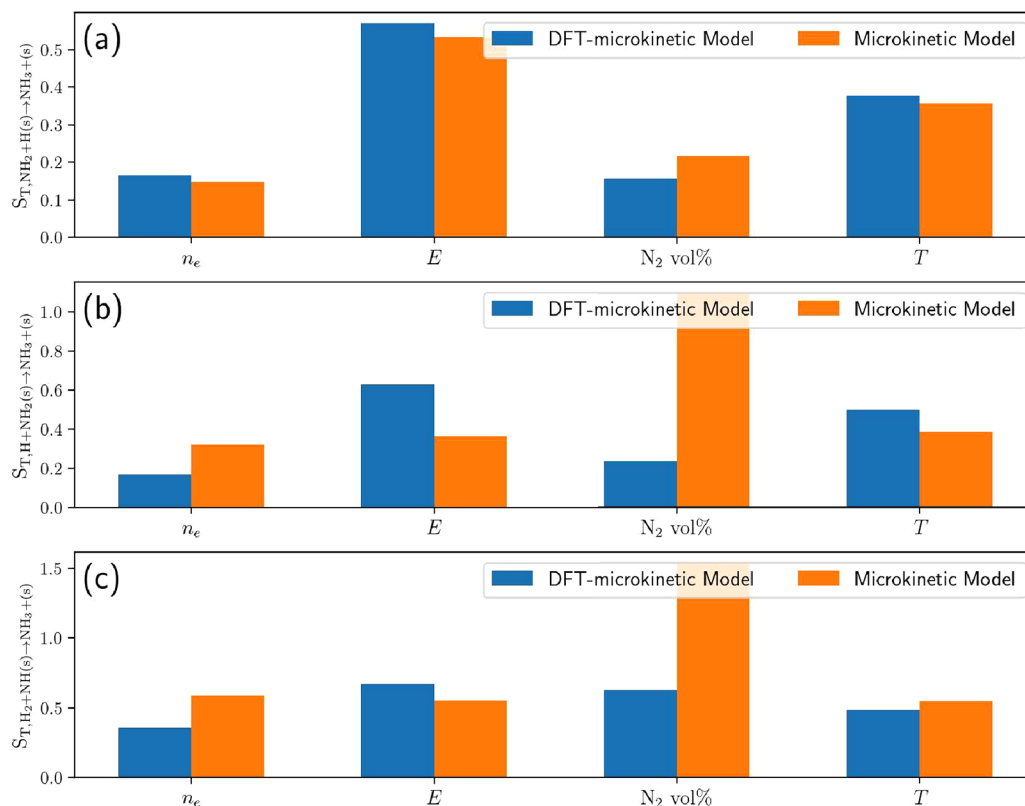
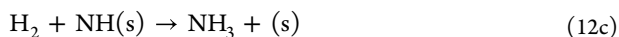
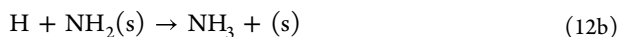
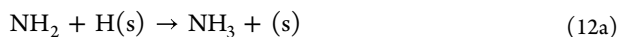


**Figure 10.** Global sensitivity analysis of rates of the three dominant reactions producing  $\text{NH}_3$  with respect to the four process parameters using the microkinetic model and the microkinetic model coupled with DFT calculations that describes the effects of electric field on the surface reactions.  $S_T$  denotes the total Sobol' indices of the reaction rates, approximated using 5000 samples. (a) Sensitivity of rate of reaction  $\text{NH}_2 + \text{H}(\text{s}) \rightarrow \text{NH}_3 + (\text{s})$ . (b) Sensitivity of rate of reaction  $\text{H} + \text{NH}_2(\text{s}) \rightarrow \text{NH}_3 + (\text{s})$ . (c) Sensitivity of rate of reaction  $\text{H}_2 + \text{NH}(\text{s}) \rightarrow \text{NH}_3 + (\text{s})$ .

density,  $n_e$ , in this model.  $n_e$  governs the probability of collisions between electrons and other particles, but its direct participation in the surface reactions has not been considered in this work. Recent DFT calculations have shown that electrons can strongly impact adsorption energies.<sup>121</sup>

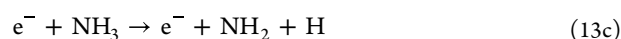
We now perform a global sensitivity analysis to investigate the impact of the four process parameters on the key reactions generating  $\text{NH}_3$ . Figure 10 shows the Sobol' indices,  $S_T$ , for the rates of reactions



with respect to the four process parameters. The E-R reactions accounting for the effects of electric field on the surface reactions clearly indicate the importance of  $E$  and  $T$  for the rates of reactions in eq 12a and eq 12b. Most notably, the significant impact of  $\text{N}_2$  vol % on the rates of reactions eq 12b and eq 12c in the microkinetic model is strongly suppressed in the DFT-microkinetic model. This reduction can be attributed to the incorporation of electric field effects through the sticking probabilities of adsorbed species that affect the E-R surface reactions. Furthermore, the global sensitivity analysis shows that  $\text{H}_2$  and  $\text{H}$  exhibit a similar sensitivity to the process parameters for both models (see Figures S2(a) and S3(a)). Additionally, although a decreased contribution of  $\text{N}_2$  vol % in the global sensitivity analysis of  $\text{NH}(\text{s})$  and  $\text{NH}_2(\text{s})$  is observed for the DFT-microkinetic model, the decrease is marginal (see Figure

S4(c,d)). Therefore, the difference in the contribution of  $\text{N}_2$  vol % between the two models for the E-R reaction in eqs 12b and 12c mainly lies in the entropy change of the reaction in eq 12b or the reaction enthalpy of the reaction in eq 12c when calculating the sticking probabilities. This is because the number densities or coverage fraction of reactants  $\text{H}_2$ ,  $\text{H}$ ,  $\text{NH}(\text{s})$ , and  $\text{NH}_2(\text{s})$  are not the primary sources of the significant  $\text{N}_2$  vol % contribution discrepancy between the DFT-microkinetic and microkinetic models. Hence, such a large contribution from  $\text{N}_2$  vol % in the microkinetic model may imply the sensitivity of reaction rates in eq 12b and eq 12c to the changes in  $\text{N}_2$  vol % is not reasonable, as experimental observations suggest that surface reactions are mainly impacted by electric field.<sup>39,116,121</sup> The increased influence of both  $E$  and  $T$  on the  $\text{NH}_3$  generation reactions via electric field effects is thus more likely.<sup>18,119,120</sup> A similar observation is also made for the reactions generating  $\text{NH}(\text{s})$ , as shown in Figure S11(b,c), where the microkinetic model predicts that  $\text{N}_2$  vol % is the most important process parameter influencing the reaction rates of  $\text{NH} + (\text{s}) \rightarrow \text{NH}(\text{s})$  and  $\text{H} + \text{N}(\text{s}) \rightarrow \text{NH}(\text{s})$ . This is while the DFT-microkinetic model correctly describes the importance of electric field.

The rates of the main reactions that dissipate energy, as discussed in the previous section, are also investigated. These reactions include



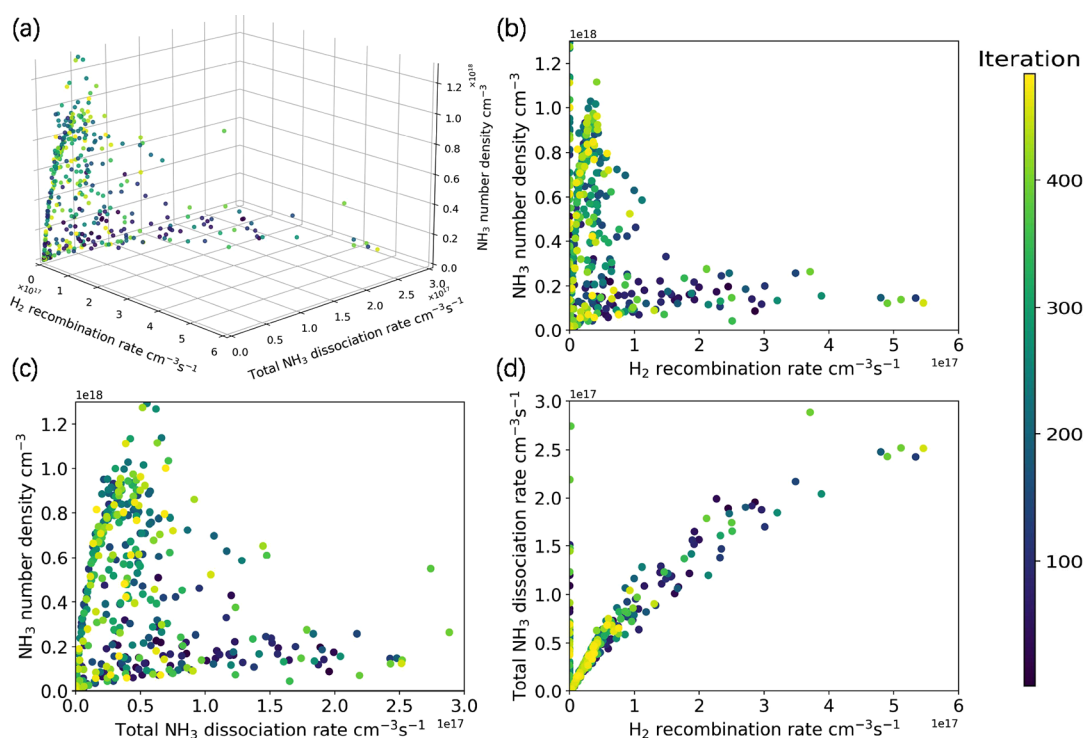
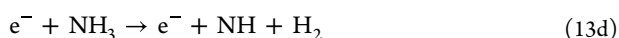


**Figure 11.** Active learning of the 4-dimensional space of process parameters based on 485 runs of the DFT-microkinetic model using multiobjective Bayesian optimization. The objectives of active learning include maximizing the  $\text{NH}_3$  number density, minimizing the total  $\text{NH}_3$  dissociation rate, and minimizing the  $\text{H}_2$  recombination rate. The latter two objectives dictate the energy efficiency of plasma-catalytic  $\text{NH}_3$  synthesis. (a) The Pareto frontier with respect to the three objectives. (b) Projection of (a) on the 2D space of the  $\text{H}_2$  recombination rate against the  $\text{NH}_3$  number density. (c) Projection of (a) on the 2D space of the total  $\text{NH}_3$  dissociation rate against the  $\text{NH}_3$  number density. (d) Projection of (a) on the 2D space of the  $\text{H}_2$  recombination rate against the total  $\text{NH}_3$  dissociation rate.

**Table 5. Seven Optimal Combinations of Process Parameters Selected from the Pareto Frontier Established Via Active Learning of the 4-Dimensional Space of Process Parameters<sup>a</sup>**

Active learning run	$T$ (K)	$n_e$ ( $\text{cm}^{-3}$ )	$E$ (V/Å)	$\text{N}_2$ vol %	$\text{NH}_3$ number density ( $\text{cm}^{-3}$ )	$\text{H}_2$ recombination rate ( $\text{cm}^{-3} \text{s}^{-1}$ )	Total $\text{NH}_3$ dissociation rate ( $\text{cm}^{-3} \text{s}^{-1}$ )
482	391.75	$5 \times 10^7$	$11.67 \times 10^{-5}$	0.909	$8.15 \times 10^{17}$	$1.24 \times 10^{16}$	$1.61 \times 10^{16}$
237	524.96	$5 \times 10^7$	$8.99 \times 10^{-5}$	0.871	$8.86 \times 10^{17}$	$1.46 \times 10^{16}$	$2.03 \times 10^{16}$
162	413.49	$5.14 \times 10^7$	$11.42 \times 10^{-5}$	0.909	$9.50 \times 10^{17}$	$1.30 \times 10^{13}$	$2.17 \times 10^{16}$
360	506.10	$5 \times 10^7$	$11.55 \times 10^{-5}$	0.881	$1.04 \times 10^{18}$	$2.10 \times 10^{14}$	$7.16 \times 10^{16}$
461	446.41	$5 \times 10^7$	$11.58 \times 10^{-5}$	0.888	$1.11 \times 10^{18}$	$4.86 \times 10^{13}$	$3.87 \times 10^{16}$
425	495.14	$5 \times 10^7$	$10.73 \times 10^{-5}$	0.859	$1.28 \times 10^{18}$	$1.13 \times 10^{14}$	$5.16 \times 10^{16}$
241	511.32	$5 \times 10^7$	$10.49 \times 10^{-5}$	0.852	$1.29 \times 10^{18}$	$1.43 \times 10^{14}$	$5.51 \times 10^{16}$

<sup>a</sup>The order of these points is based on the achieved  $\text{NH}_3$  number density.



Except for the  $\text{N}_2$  recombination reaction in eq 13a, only small variations in the Sobol' indices of the rates of these reactions are observed with respect to the changes of the process parameters, as shown in Figure S13. For the reaction in eq 13a, the electric field effects outweigh the impact of  $\text{N}_2$  vol %. This is plausible since the number density of N is usually small due to the limited dissociation of  $\text{N}_2$  in the gas phase, which in turn results in a large translational entropy barrier for the reaction to happen. Therefore, the dependence of the rate of the reaction in eq 13a on  $\text{N}_2$  vol % is expected to be relatively small. As for the reaction in eq 13b, the small variation in the Sobol' indices is attributed to the abundance of H and H(s), causing the reaction rate to be almost identical under both models. We note that  $n_e$  is much less important than  $E$  and  $T$  for the rates of reactions eq 13c and eq 13d, contrary to the findings that  $n_e$  is critical to the energy dissipation via  $\text{e}^-$  and  $\text{NH}_3$  collisions.<sup>25</sup>

### Optimal Trade-off between $\text{NH}_3$ Production and Energy Efficiency

As evident from the above discussion, the four process parameters considered in this work influence the gas-phase and surface reactions in highly nonlinear and interdependent ways, which poses a major challenge to maximizing  $\text{NH}_3$  production. This challenge is further compounded when striving to minimize the rates of energy-dissipating reactions in order to enhance the overall energy efficiency of the process. We use active learning to systematically investigate how the four process parameters influence the trade-off between the conflicting objectives of maximizing  $\text{NH}_3$  production (i.e.,  $\text{NH}_3$  number density) and minimizing the rates of energy-dissipating reactions. Energy dissipation is evaluated based on the rates of  $\text{NH}_3$  dissociation reactions (eqs 13c and 13d) and the rate of  $\text{H}_2$  recombination reaction (eq 13b). As such, the active learning problem is formulated as a multiobjective Bayesian optimization

problem with three objectives: maximizing the  $\text{NH}_3$  number density, minimizing the total  $\text{NH}_3$  dissociation rate, and minimizing the  $\text{H}_2$  recombination rate. Note that the  $\text{N}_2$  recombination reaction in eq 13a is not considered because its rate is usually much lower than that of the  $\text{H}_2$  recombination reaction in eq 13b due to the low number densities of N and N(s). The  $\text{N}_2$  recombination rate is only comparable to that of  $\text{H}_2$  recombination when  $\text{N}_2$  vol % reaches at least 97%, under which case the  $\text{NH}_3$  number density is usually very small.

Figure 11 depicts the outcome of active learning of the 4-dimensional (4D) space of process parameters based on 485 runs of the DFT-microkinetic model wherein the three objectives are evaluated at 4000 s. As can be seen, to obtain a higher number density of  $\text{NH}_3$ , the reaction rates of both  $\text{H}_2$  recombination and  $\text{NH}_3$  dissociation must increase. The active learning of the parameter space yields a Pareto frontier, which consists of a set of process parameters that are optimal with respect to the three objectives considered in the multiobjective Bayesian optimization problem.

Table 5 lists seven optimal process parameters selected from the Pareto frontier, where the  $\text{NH}_3$  number density has a favorable value of approximately  $10^8 \text{ cm}^{-3}$ . To maximize the  $\text{NH}_3$  number density while suppressing the energy-dissipating reactions, electron number density is pushed to its lower bound and  $\text{N}_2$  vol % is maintained at a relatively higher level. This is because  $n_e$  directly controls the reaction rate of  $\text{NH}_3$  decomposition by collision with  $e^-$ , as also observed by Hong et al.<sup>25,49</sup> On the other hand, the suggested values for  $\text{N}_2$  vol % by active learning, in the range of 0.85 to 0.9, can significantly decrease the number density of H and H(s) for the reaction in eq 13b, while not limiting the generation of  $\text{NH}_3$  and avoiding a large energy dissipation caused by  $\text{N}_2$  recombination. The optimal process parameters in runs 241 and 425 yield the largest  $\text{NH}_3$  number density. Although the resulting process parameters in these two runs are very similar, the small variations in  $T$ ,  $E$ , and  $\text{N}_2$  vol % can result in an increase of 6.78% in the total  $\text{NH}_3$  dissociation rate and an increase of 26.55% in the  $\text{H}_2$  recombination rate. Hence, the small improvement in  $\text{NH}_3$  production is associated with a fairly large increase in the rates of energy-dissipating reactions, which diminishes the energy efficiency of  $\text{NH}_3$  synthesis. This analysis illustrates the highly complex and nonlinear relationships between the process parameters and  $\text{NH}_3$  production and its energy efficiency, where even small changes in the input process parameters can lead to vastly different process outcomes. Furthermore, this study shows the promise of active learning for systematic and computationally efficient exploration of the complex parameter space of plasma-catalytic systems with multiple objectives.

## CONCLUSIONS AND FUTURE WORK

This paper investigated how process parameters, including electric field, reactor temperature, inlet  $\text{N}_2$  vol %, and electron number density, can influence plasma-catalytic ammonia synthesis in a cylindrical dielectric barrier discharge reactor packed with Fe(110) catalysts. A first-principles framework that integrates DFT with microkinetic modeling is used to account for the impact of electric field on surface reactions. We observed that electric field and reactor temperature can influence reaction rates in a nonlinear manner, possibly leading to changes in the  $\text{NH}_3$  synthesis reaction pathways. A global sensitivity analysis illustrated that the predictions of the DFT-microkinetic model are consistent with experimental observations from the literature, as compared to a microkinetic model that disregards

the effect of electric field on surface reactions. Additionally, the global sensitivity analysis elucidated the contributions of the process parameters to the generation/loss of gas-phase and surface species, providing insights for further improvement of microkinetic models and informing the design of plasma-catalytic reactors for ammonia synthesis. Finally, we used multiobjective Bayesian optimization to systematically investigate the trade-off between  $\text{NH}_3$  production and its energy efficiency. Notably, we observed that similar combinations of process parameters yielding comparable  $\text{NH}_3$  production can result in vastly different energy dissipation via  $\text{NH}_3$  dissociation and  $\text{H}_2$  recombination reactions. This observation underscores the complexity and sensitivity of plasma-catalytic processes to their input parameters.

To the best of our knowledge, this work is the first effort to combine microkinetic modeling with DFT to investigate the effects of electric field on plasma-catalyst interactions. Nonetheless, the potential effects of other plasma-surface interactions, including surface accumulated charges, photons, and surface morphological alterations, were not accounted for in this work. In addition, further research is warranted to investigate how the presence of electric field, as well as other plasma-surface interactions, may influence diffusion activation energies and activation energies of the surface reactions. To this end, more sophisticated and computationally demanding techniques, such as time-dependent density functional theory, hold promise for establishing a more comprehensive view of how activation energies and entropic changes may be influenced by vibrationally excited species, exemplified by  $\text{N}_2(\nu_1)$ . These avenues can provide a deeper understanding of the intricate interactions at play in plasma-catalytic processes and pave the way for enhanced control and optimization of these processes.

## DATA AVAILABILITY STATEMENT

**Codes.** The scripts for DFT calculations, microkinetic model, and multiobjective Bayesian optimization can be found in <https://github.com/wwwcctoo/DFT-microkinetic>.

## ASSOCIATED CONTENT

### Supporting Information

The Supporting Information is available free of charge at <https://pubs.acs.org/doi/10.1021/jacsau.3c00654>.

Details about the parameters of the DFT-microkinetic model, the optimized structure, and other comparisons between predictions of the microkinetic model adopted from ref 25 and the presented DFT-microkinetic model (PDF)

## AUTHOR INFORMATION

### Corresponding Author

Ali Mesbah – Department of Chemical & Biomolecular Engineering, University of California, Berkeley, California 94720, United States; [orcid.org/0000-0002-1700-0600](https://orcid.org/0000-0002-1700-0600); Email: [mesbah@berkeley.edu](mailto:mesbah@berkeley.edu)

### Author

Ketong Shao – Department of Chemical & Biomolecular Engineering, University of California, Berkeley, California 94720, United States; [orcid.org/0000-0002-6104-2509](https://orcid.org/0000-0002-6104-2509)

Complete contact information is available at <https://pubs.acs.org/10.1021/jacsau.3c00654>

## Notes

The authors declare no competing financial interest.

### ACKNOWLEDGMENTS

This material is based upon work supported by the U.S. Department of Energy, Office of Science, Office of Fusion Energy Sciences under award number DE-SC0020232. This work used SDSC Expanse CPU and SDSC Expanse Projects Storage at San Diego Supercomputer Center (SDSC) through allocation CHM220008 from the Advanced Cyberinfrastructure Coordination Ecosystem: Services & Support (ACCESS) program, which is supported by the National Science Foundation grants #2138259, #2138286, #2138307, #2137603, and #2138296.

### NOMENCLATURE

$E$ , V/Å; Electric field  
 $E_{\text{surf}}$ , V/Å; Surface electric field  
 $E_r$ , Td; Reduced electric field  
 $T$ , K; Gas temperature (Catalyst temperature is assumed to be the same as gas temperature.)  
 $p$ , atm; Pressure  
 $n_t$ ,  $\text{cm}^{-3}$ ; Total species number density in gas phase  
 $N_i$ ; Number of  $i^{\text{th}}$  species  
 $n_i$ ,  $\text{cm}^{-3}$ ; Number density of  $i^{\text{th}}$  species  
 $n_e$ ,  $\text{cm}^{-3}$ ; Electron number density  
 $T_e$ , K; Electron temperature  
 $R_j$ ,  $\text{cm}^{-3} \text{ s}^{-1}$ ; Rate of  $j^{\text{th}}$  reaction  
 $E_a$ , eV; Activation energy  
 $E_d$ , eV; Diffusion activation energy  
 $S_T$ ,  $\text{cm}^{-2}$ ; Density of total surface sites  
 $\Delta H$ , eV; Enthalpy of a reaction  
 $V$ ,  $\text{cm}^3$ ; Discharge volume  
 $A$ ,  $\text{cm}^2$ ; Catalyst surface area  
 $\gamma$ ; Sticking probability for direct adsorption  
 $\gamma_{\text{ER}}$ ; Sticking probability for E-R reactions  
 $\gamma_{\text{std}}$ ; Sticking probability defined under standard conditions for E-R reactions  
 $\bar{p}$ , atm; Partial pressure of the reactant gas species in E-R reactions  
 $\bar{p}_{\text{std}}$ , atm;  $\bar{p}$  under standard conditions of the reactant gas species in E-R reactions  
 $S_{\text{gas}}$ ,  $\text{J K}^{-1} \text{ mol}^{-1}$ ; Gas-phase species entropy  
 $S_{\text{ads}}$ ,  $\text{J K}^{-1} \text{ mol}^{-1}$ ; Adsorbed species entropy  
 $\Delta S$ ,  $\text{J K}^{-1} \text{ mol}^{-1}$ ; Entropy change of a reaction  
 $\Delta S_{\text{std}}$ ,  $\text{J K}^{-1} \text{ mol}^{-1}$ ; Entropy change of a reaction defined under standard conditions

### ADDITIONAL NOTE

<sup>a</sup>It should be noted that this study does not encompass the investigation of different catalyst materials, or the role of catalyst support.

### REFERENCES

- Gross, M. Human population at the crossroads. *Curr. Biol.* **2023**, *33*, R1–R3.
- Rees, W. E.; et al. The human eco-predicament: Overshoot and the population conundrum. In *Vienna Yearbook of Population Research*; Verlag der Österreichischen Akademie der Wissenschaften, 2023; pp 21.
- Erisman, J. W.; Sutton, M. A.; Galloway, J.; Klimont, Z.; Winiwarter, W. How a century of ammonia synthesis changed the world. *Nature Geoscience* **2008**, *1*, 636–639.
- Sun, J.; Alam, D.; Daiyan, R.; Masood, H.; Zhang, T.; Zhou, R.; Cullen, P. J.; Lovell, E. C.; Jalili, A. R.; Amal, R. A hybrid plasma electrocatalytic process for sustainable ammonia production. *Energy Environ. Sci.* **2021**, *14*, 865–872.
- Kandemir, T.; Schuster, M. E.; Senyshyn, A.; Behrens, M.; Schlögl, R. The Haber–Bosch process revisited: on the real structure and stability of “ammonia iron” under working conditions. *Angew. Chem., Int. Ed.* **2013**, *52*, 12723–12726.
- Pfromm, P. H. Towards sustainable agriculture: Fossil-free ammonia. *Journal of Renewable and Sustainable Energy* **2017**, *9*, 034702.
- Smith, C.; Hill, A. K.; Torrente-Murciano, L. Current and future role of Haber–Bosch ammonia in a carbon-free energy landscape. *Energy Environ. Sci.* **2020**, *13*, 331–344.
- Kyriakou, V.; Garagounis, I.; Vourros, A.; Vasileiou, E.; Stoukides, M. An electrochemical haber-bosch process. *Joule* **2020**, *4*, 142–158.
- Liu, Q.; Xu, T.; Luo, Y.; Kong, Q.; Li, T.; Lu, S.; Alshehri, A. A.; Alzahrani, K. A.; Sun, X. Recent advances in strategies for highly selective electrocatalytic  $\text{N}_2$  reduction toward ambient  $\text{NH}_3$  synthesis. *Current Opinion in Electrochemistry* **2021**, *29*, 100766.
- Yan, Z.; Ji, M.; Xia, J.; Zhu, H. Recent advanced materials for electrochemical and photoelectrochemical synthesis of ammonia from dinitrogen: One step closer to a sustainable energy future. *Adv. Energy Mater.* **2020**, *10*, 1902020.
- Mingdong, B.; Xiyao, B.; Zhitao, Z.; Mindi, B. Synthesis of ammonia in a strong electric field discharge at ambient pressure. *Plasma Chemistry and Plasma Processing* **2000**, *20*, 511–520.
- Chen, H.; Yuan, D.; Wu, A.; Lin, X.; Li, X. Review of low-temperature plasma nitrogen fixation technology. *Waste Disposal & Sustainable Energy* **2021**, *3*, 201–217.
- Patil, B.; Wang, Q.; Hessel, V.; Lang, J. Plasma  $\text{N}_2$ -fixation: 1900–2015. *Catalysis today* **2015**, *256*, 49–66.
- Wang, W.; Patil, B.; Heijkers, S.; Hessel, V.; Bogaerts, A. Nitrogen fixation by gliding arc plasma: better insight by chemical kinetics modelling. *ChemSusChem* **2017**, *10*, 2145–2157.
- Lamichhane, P.; Veerana, M.; Lim, J. S.; Mumtaz, S.; Shrestha, B.; Kaushik, N. K.; Park, G.; Choi, E. H. Low-temperature plasma-assisted nitrogen fixation for corn plant growth and development. *International Journal of Molecular Sciences* **2021**, *22*, 5360.
- Patil, B.; Wang, Q.; Hessel, V.; Lang, J. Plasma-assisted nitrogen fixation reactions. In *Alternative Energy Sources for Green Chemistry*; Royal Society of Chemistry, 2016; pp 296–338.
- Mehta, P.; Barboun, P.; Herrera, F. A.; Kim, J.; Rumbach, P.; Go, D. B.; Hicks, J. C.; Schneider, W. F. Overcoming ammonia synthesis scaling relations with plasma-enabled catalysis. *Nature Catalysis* **2018**, *1*, 269–275.
- Rouwenhorst, K. H. R.; Burbach, H. G. B.; Vogel, D. W.; Nunez Pauli, J.; Geerdink, B.; Lefferts, L. Plasma-catalytic ammonia synthesis beyond thermal equilibrium on Ru-based catalysts in non-thermal plasma. *Catalysis science & technology* **2021**, *11*, 2834–2843.
- Barboun, P. M.; Daemen, L. L.; Waitt, C.; Wu, Z.; Schneider, W. F.; Hicks, J. C. Inelastic neutron scattering observation of plasma-promoted nitrogen reduction intermediates on Ni/ $\gamma$ - $\text{Al}_2\text{O}_3$ . *ACS Energy Letters* **2021**, *6*, 2048–2053.
- Carreon, M. L. Plasma catalytic ammonia synthesis: state of the art and future directions. *J. Phys. D: Appl. Phys.* **2019**, *52*, 483001.
- Wang, Y.; Craven, M.; Yu, X.; Ding, J.; Bryant, P.; Huang, J.; Tu, X. Plasma-enhanced catalytic synthesis of ammonia over a Ni/ $\text{Al}_2\text{O}_3$  catalyst at near-room temperature: insights into the importance of the catalyst surface on the reaction mechanism. *ACS catalysis* **2019**, *9*, 10780–10793.
- Tu, X.; Whitehead, J. Plasma-catalytic dry reforming of methane in an atmospheric dielectric barrier discharge: Understanding the synergistic effect at low temperature. *Applied Catalysis B: Environmental* **2012**, *125*, 439–448.
- Wang, L.; Yi, Y.; Zhao, Y.; Zhang, R.; Zhang, J.; Guo, H.  $\text{NH}_3$  decomposition for  $\text{H}_2$  generation: effects of cheap metals and supports on plasma–catalyst synergy. *ACS Catal.* **2015**, *5*, 4167–4174.

- (24) Kim, J.; Go, D. B.; Hicks, J. C. Synergistic effects of plasma–catalyst interactions for CH<sub>4</sub> activation. *Phys. Chem. Chem. Phys.* **2017**, *19*, 13010–13021.
- (25) Hong, J.; Pancheshnyi, S.; Tam, E.; Lowke, J. J.; Prawer, S.; Murphy, A. B. Kinetic modelling of NH<sub>3</sub> production in N<sub>2</sub>–H<sub>2</sub> non-equilibrium atmospheric-pressure plasma catalysis. *J. Phys. D: Appl. Phys.* **2017**, *50*, 154005.
- (26) Bogaerts, A.; Tu, X.; Whitehead, J. C.; Centi, G.; Lefferts, L.; Guaitella, O.; Azzolina-Jury, F.; Kim, H. H.; Murphy, A. B.; Schneider, W. F.; et al. The 2020 plasma catalysis roadmap. *J. Phys. D: Appl. Phys.* **2020**, *53*, 443001.
- (27) Liu, T.-W.; Gorky, F.; Carreon, M. L.; Gómez-Gualdrón, D. A. Energetics of reaction pathways enabled by N and H radicals during catalytic, plasma-assisted NH<sub>3</sub> synthesis. *ACS Sustainable Chem. Eng.* **2022**, *10*, 2034–2051.
- (28) Pancheshnyi, S.; Eismann, B.; Hagelaar, G.; Pitchford, L. *Computer code ztplaskin*; University of Toulouse, LAPLACE, CNRS-UPS-INP: Toulouse, France, 2008.
- (29) Engelmann, Y.; van't Veer, K.; Gorbanev, Y.; Neyts, E. C.; Schneider, W. F.; Bogaerts, A. Plasma Catalysis for Ammonia Synthesis: A Microkinetic Modeling Study on the Contributions of Eley–Rideal Reactions. *ACS Sustainable Chem. Eng.* **2021**, *9*, 13151–13163.
- (30) Adamovich, I.; Agarwal, S.; Ahedo, E.; Alves, L. L.; Baalrud, S.; Babaeva, N.; Bogaerts, A.; Bourdon, A.; Bruggeman, P.; Canal, C.; et al. The 2022 Plasma Roadmap: low temperature plasma science and technology. *J. Phys. D: Appl. Phys.* **2022**, *55*, 373001.
- (31) Whitehead, J. C. Plasma–catalysis: the known knowns, the known unknowns and the unknown unknowns. *J. Phys. D: Appl. Phys.* **2016**, *49*, 243001.
- (32) Doherty, F.; Goldsmith, B. R. Modeling plasma-induced surface charge effects on CO<sub>2</sub> activation by single atom catalysts supported on reducible and irreducible metal oxides. *Plasma Sources Science and Technology* **2023**, *32*, 034004.
- (33) Zhao, H.; Song, G.; Chen, Z.; Yang, X.; Yan, C.; Abe, S.; Ju, Y.; Sundaresan, S.; Koel, B. E. In situ identification of NNH and N<sub>2</sub>H<sub>2</sub> by using molecular-beam mass spectrometry in plasma-assisted catalysis for NH<sub>3</sub> synthesis. *ACS Energy Letters* **2022**, *7*, 53–58.
- (34) Wang, Y.; Yang, W.; Xu, S.; Zhao, S.; Chen, G.; Weidenkaff, A.; Hardacre, C.; Fan, X.; Huang, J.; Tu, X. Shielding protection by mesoporous catalysts for improving plasma-catalytic ambient ammonia synthesis. *J. Am. Chem. Soc.* **2022**, *144*, 12020–12031.
- (35) Xu, L.; Kirvassilis, D.; Bai, Y.; Mavrikakis, M. Atomic and molecular adsorption on Fe (110). *Surf. Sci.* **2018**, *667*, 54–65.
- (36) Logadottir, A.; Rod, T. H.; Nørskov, J. K.; Hammer, B.; Dahl, S.; Jacobsen, C. The Bronsted–Evans–Polanyi relation and the volcano plot for ammonia synthesis over transition metal catalysts. *J. Catal.* **2001**, *197*, 229–231.
- (37) Mittasch, A.; Frankenburg, W. *Advances in Catalysis*; Elsevier, 1950; Vol. 2; pp 81–104.
- (38) Jacobsen, C. J.; Dahl, S.; Clausen, B. S.; Bahn, S.; Logadottir, A.; Nørskov, J. K. Catalyst design by interpolation in the periodic table: bimetallic ammonia synthesis catalysts. *J. Am. Chem. Soc.* **2001**, *123*, 8404–8405.
- (39) Winter, L. R.; Ashford, B.; Hong, J.; Murphy, A. B.; Chen, J. G. Identifying surface reaction intermediates in plasma catalytic ammonia synthesis. *ACS Catal.* **2020**, *10*, 14763–14774.
- (40) Shah, J.; Wang, W.; Bogaerts, A.; Carreon, M. L. Ammonia synthesis by radio frequency plasma catalysis: revealing the underlying mechanisms. *ACS Applied Energy Materials* **2018**, *1*, 4824–4839.
- (41) Carrasco, E.; Jiménez-Redondo, M.; Tanarro, I.; Herrero, V. J. Neutral and ion chemistry in low pressure dc plasmas of H<sub>2</sub>/N<sub>2</sub> mixtures: routes for the efficient production of NH<sub>3</sub> and NH<sub>4</sub><sup>+</sup>. *Phys. Chem. Chem. Phys.* **2011**, *13*, 19561–19572.
- (42) Gunantara, N. A review of multi-objective optimization: Methods and its applications. *Cogent Engineering* **2018**, *5*, 1502242.
- (43) Laumanns, M.; Ocenasek, J. Bayesian optimization algorithms for multi-objective optimization, September 7–11, 2002, Granada, Spain. In *Proceedings Parallel Problem Solving from Nature-PPSN VII: 7th International Conference*; SpringerLink, 2002; Vol. 2439, pp 298–307.
- (44) Shao, K.; Pei, X.; Graves, D. B.; Mesbah, A. Active learning-guided exploration of parameter space of air plasmas to enhance the energy efficiency of NO<sub>x</sub> production. *Plasma Sources Science and Technology* **2022**, *31*, 055018.
- (45) Makrygiorgos, G.; Bonzanini, A. D.; Miller, V.; Mesbah, A. Performance-oriented model learning for control via multi-objective Bayesian optimization. *Comput. Chem. Eng.* **2022**, *162*, 107770.
- (46) Bonzanini, A. D.; Shao, K.; Graves, D. B.; Hamaguchi, S.; Mesbah, A. Foundations of machine learning for low-temperature plasmas: methods and case studies. *Plasma Sources Science and Technology* **2023**, *32*, 024003.
- (47) Hagelaar, G.; Pitchford, L. C. Solving the Boltzmann equation to obtain electron transport coefficients and rate coefficients for fluid models. *Plasma sources science and technology* **2005**, *14*, 722.
- (48) Estepa, A. L.; Pannier, E.; Ivko, S. *QtPlaskin*. 2022; <https://github.com/erwanp/qtplaskin>, (Last Accessed 2022-05).
- (49) Hong, J.; Prawer, S.; Murphy, A. B. Plasma catalysis as an alternative route for ammonia production: status, mechanisms, and prospects for progress. *ACS Sustainable Chem. Eng.* **2018**, *6*, 15–31.
- (50) Hong, J.; Prawer, S.; Murphy, A. B. Production of ammonia by heterogeneous catalysis in a packed-bed dielectric-barrier discharge: influence of argon addition and voltage. *IEEE Transactions on Plasma Science* **2014**, *42*, 2338–2339.
- (51) Andersen, J.; Christensen, J.; Østberg, M.; Bogaerts, A.; Jensen, A. Plasma-catalytic ammonia decomposition using a packed-bed dielectric barrier discharge reactor. *international journal of hydrogen energy* **2022**, *47*, 32081–32091.
- (52) Kang, W. S.; Park, J. M.; Kim, Y.; Hong, S. H. Numerical study on influences of barrier arrangements on dielectric barrier discharge characteristics. *IEEE Transactions on Plasma Science* **2003**, *31*, 504–510.
- (53) Liu, C.; Fridman, A.; Dobrynin, D. Investigation of the transition from streamer to uniform ‘overvoltage’ mode of atmospheric air nanosecond-pulsed dielectric barrier discharge. *J. Phys. D: Appl. Phys.* **2019**, *52*, 105205.
- (54) Van't Veer, K.; Reniers, F.; Bogaerts, A. Zero-dimensional modeling of unpacked and packed bed dielectric barrier discharges: the role of vibrational kinetics in ammonia synthesis. *Plasma Sources Sci. Technol.* **2020**, *29*, 045020.
- (55) Barth, J. V. Transport of adsorbates at metal surfaces: from thermal migration to hot precursors. *Surf. Sci. Rep.* **2000**, *40*, 75–149.
- (56) Cortright, R.; Dumesic, J. Kinetics of heterogeneous catalytic reactions: Analysis of reaction schemes. *Adv. Catal.* **2001**, *46*, 161–264.
- (57) Durant, J. L. Evaluation of transition state properties by density functional theory. *Chemical physics letters* **1996**, *256*, 595–602.
- (58) Henkelman, G.; Uberuaga, B. P.; Jónsson, H. A climbing image nudged elastic band method for finding saddle points and minimum energy paths. *J. Chem. Phys.* **2000**, *113*, 9901–9904.
- (59) Wallington, T.; Kaiser, E.; Farrell, J. Automotive fuels and internal combustion engines: a chemical perspective. *Chem. Soc. Rev.* **2006**, *35*, 335–347.
- (60) Roberts, B. P.; Steel, A. J. An extended form of the Evans–Polanyi equation: a simple empirical relationship for the prediction of activation energies for hydrogen-atom transfer reactions. *J. Chem. Soc., Perkin Trans.* **1994**, *2*, 2155–2162.
- (61) Evans, M.; Polanyi, M. Further considerations on the thermodynamics of chemical equilibria and reaction rates. *Trans. Faraday Soc.* **1936**, *32*, 1333–1360.
- (62) Evans, M.; Polanyi, M. Inertia and driving force of chemical reactions. *Trans. Faraday Soc.* **1938**, *34*, 11–24.
- (63) Cohen, N.; Benson, S. Estimation of heats of formation of organic compounds by additivity methods. *Chem. Rev.* **1993**, *93*, 2419–2438.
- (64) Cohen, N. The use of transition-state theory to extrapolate rate coefficients for reactions of H atoms with alkanes. *International journal of chemical kinetics* **1991**, *23*, 683–700.
- (65) Bell, R. P. The theory of reactions involving proton transfers. *Proceedings of the Royal Society of London. Series A-Mathematical and Physical Sciences* **1936**, *154*, 414–429.

- (66) Che, F.; Gray, J. T.; Ha, S.; McEwen, J.-S. Improving Ni catalysts using electric fields: a DFT and experimental study of the methane steam reforming reaction. *ACS Catal.* **2017**, *7*, 551–562.
- (67) Wang, S.; Petzold, V.; Tripkovic, V.; Kleis, J.; Howalt, J. G.; Skulason, E.; Fernandez, E.; Hvolbæk, B.; Jones, G.; Toftelund, A.; et al. Universal transition state scaling relations for (de) hydrogenation over transition metals. *Phys. Chem. Chem. Phys.* **2011**, *13*, 20760–20765.
- (68) Chen, Z.; Koel, B. E.; Sundaresan, S. Plasma-assisted catalysis for ammonia synthesis in a dielectric barrier discharge reactor: key surface reaction steps and potential causes of low energy yield. *J. Phys. D: Appl. Phys.* **2022**, *55*, 055202.
- (69) Murphy, A. A comparison of treatments of diffusion in thermal plasmas. *J. Phys. D: Appl. Phys.* **1996**, *29*, 1922.
- (70) Hays, G.; Tracy, C.; Oskam, H. Surface catalytic efficiency of a sputtered molybdenum layer on quartz and Pyrex for the recombination of nitrogen atoms. *J. Chem. Phys.* **1974**, *60*, 2027–2034.
- (71) Mortensen, J. J.; Hansen, L. B.; Hammer, B.; Nørskov, J. K. Nitrogen adsorption and dissociation on Fe (111). *J. Catal.* **1999**, *182*, 479–488.
- (72) Loenders, B.; Engelmann, Y.; Bogaerts, A. Plasma-catalytic partial oxidation of methane on Pt (111): a microkinetic study on the role of different plasma species. *J. Phys. Chem. C* **2021**, *125*, 2966–2983.
- (73) Waitt, C.; Miles, A. R.; Schneider, W. F. Adsorbate free energies from DFT-derived translational energy landscapes. *J. Phys. Chem. C* **2021**, *125*, 20331–20342.
- (74) Campbell, C. T.; Sellers, J. R. The entropies of adsorbed molecules. *J. Am. Chem. Soc.* **2012**, *134*, 18109–18115.
- (75) Jiménez-Redondo, M.; Carrasco, E.; Herrero, V. J.; Tanarro, I. Isotopic exchange processes in cold plasmas of H<sub>2</sub>/D<sub>2</sub> mixtures. *Phys. Chem. Chem. Phys.* **2011**, *13*, 9655–9666.
- (76) Ertl, G. Surface science and catalysis—studies on the mechanism of ammonia synthesis: the PH Emmett award address. *Catalysis Reviews Science and Engineering* **1980**, *21*, 201–223.
- (77) Lieberman, M. A.; Lichtenberg, A. J. *Principles of plasma discharges and materials processing*; John Wiley & Sons, 2005.
- (78) Hansen, F. Y.; Henriksen, N. E.; Billing, G. D.; Guldborg, A. Catalytic synthesis of ammonia using vibrationally excited nitrogen molecules: theoretical calculation of equilibrium and rate constants. *Surface science* **1992**, *264*, 225–234.
- (79) Billing, G. D.; Guldborg, A.; Henriksen, N. E.; Hansen, F. Y. Dissociative chemisorption of N<sub>2</sub> on rhenium: dynamics at low impact energies. *Chemical physics* **1990**, *147*, 1–11.
- (80) Rettner, C.; Stein, H. Effect of vibrational energy on the dissociative chemisorption of N<sub>2</sub> on Fe (111). *J. Chem. Phys.* **1987**, *87*, 770–771.
- (81) Kresse, G.; Hafner, J. Ab initio molecular dynamics for liquid metals. *Phys. Rev. B* **1993**, *47*, 558.
- (82) Kresse, G.; Furthmüller, J. Efficiency of ab-initio total energy calculations for metals and semiconductors using a plane-wave basis set. *Computational materials science* **1996**, *6*, 15–50.
- (83) Giannozzi, P.; Baroni, S.; Bonini, N.; Calandra, M.; Car, R.; Cavazzoni, C.; Ceresoli, D.; Chiarotti, G. L.; Cococcioni, M.; Dabo, I.; et al. QUANTUM ESPRESSO: a modular and open-source software project for quantum simulations of materials. *J. Phys.: Condens. Matter* **2009**, *21*, 395502.
- (84) Hjorth Larsen, A.; Jorgen Mortensen, J.; Blomqvist, J.; Castelli, I. E.; Christensen, R.; Dulak, M.; Friis, J.; Groves, M. N.; Hammer, B.; Hargus, C.; et al. The atomic simulation environment—a Python library for working with atoms. *J. Phys.: Condens. Matter* **2017**, *29*, 273002.
- (85) Boerner, T. J.; Deems, S.; Furlani, T. R.; Knuth, S. L.; Towns, J. ACCESS: Advancing Innovation: NSF's Advanced Cyberinfrastructure Coordination Ecosystem: Services & Support. In *Practice and Experience in Advanced Research Computing Association for Computing Machinery*; New York, NY, 2023, 173–176, DOI: 10.1145/3569951.3597559.
- (86) Perdew, J. P.; Burke, K.; Ernzerhof, M. Generalized gradient approximation made simple. *Physical review letters* **1996**, *77*, 3865.
- (87) Prandini, G.; Marrazzo, A.; Castelli, I. E.; Mounet, N.; Marzari, N. Precision and efficiency in solid-state pseudopotential calculations. *npj Comput. Mater.* **2018**, *4*, 1–13.
- (88) Bucko, T.; Hafner, J.; Lebegue, S.; Angyan, J. G. Improved description of the structure of molecular and layered crystals: ab initio DFT calculations with van der Waals corrections. *J. Phys. Chem. A* **2010**, *114*, 11814–11824.
- (89) Grimme, S. Semiempirical GGA-type density functional constructed with a long-range dispersion correction. *Journal of computational chemistry* **2006**, *27*, 1787–1799.
- (90) Kerber, T.; Sierka, M.; Sauer, J. Application of semiempirical long-range dispersion corrections to periodic systems in density functional theory. *Journal of computational chemistry* **2008**, *29*, 2088–2097.
- (91) *PW Input File Description*. [https://www.quantum-espresso.org/Doc/INPUT\\_PW.html](https://www.quantum-espresso.org/Doc/INPUT_PW.html), (Last Accessed 2022-01).
- (92) Methfessel, M.; Paxton, A. High-precision sampling for Brillouin-zone integration in metals. *physical review B* **1989**, *40*, 3616.
- (93) Mattsson, A. E.; Armiento, R.; Schultz, P. A.; Mattsson, T. R. Nonequivalence of the generalized gradient approximations PBE and PW91. *Phys. Rev. B* **2006**, *73*, 195123.
- (94) Otani, M.; Sugino, O. First-principles calculations of charged surfaces and interfaces: A plane-wave nonrepeated slab approach. *Phys. Rev. B* **2006**, *73*, 115407.
- (95) Hamada, I.; Sugino, O.; Bonnet, N.; Otani, M. Improved modeling of electrified interfaces using the effective screening medium method. *Phys. Rev. B* **2013**, *88*, 155427.
- (96) Resta, R.; Vanderbilt, D. *Physics of Ferroelectrics*; Springer, 2007; pp 31–68.
- (97) Hong, J.; Aramesh, M.; Shimoni, O.; Seo, D. H.; Yick, S.; Greig, A.; Charles, C.; Prawer, S.; Murphy, A. B. Plasma catalytic synthesis of ammonia using functionalized-carbon coatings in an atmospheric-pressure non-equilibrium discharge. *Plasma Chemistry and Plasma Processing* **2016**, *36*, 917–940.
- (98) Edgcombe, C.; Valdre, U. Microscopy and computational modelling to elucidate the enhancement factor for field electron emitters. *J. Microsc.* **2001**, *203*, 188–194.
- (99) Kaushik, V.; Shukla, A.; Vankar, V. Microwave plasma CVD-grown graphene–CNT hybrids for enhanced electron field emission applications. *Appl. Phys. A: Mater. Sci. Process.* **2014**, *117*, 2197–2205.
- (100) Neyts, E. C. Plasma-surface interactions in plasma catalysis. *Plasma chemistry and plasma processing* **2016**, *36*, 185–212.
- (101) Sobol, I. M. Sensitivity analysis for non-linear mathematical models. *Mathematical modelling and computational experiment* **1993**, *1*, 407–414.
- (102) Sudret, B. Global sensitivity analysis using polynomial chaos expansions. *Reliability engineering & system safety* **2008**, *93*, 964–979.
- (103) Saltelli, A.; Tarantola, S.; Chan, K.-S. A quantitative model-independent method for global sensitivity analysis of model output. *Technometrics* **1999**, *41*, 39–56.
- (104) Herman, J.; Usher, W. SALib: An open-source Python library for Sensitivity Analysis. *JOSS* **2017**, *2*, 97.
- (105) Campolongo, F.; Saltelli, A.; Cariboni, J. From screening to quantitative sensitivity analysis. A unified approach. *Comput. Phys. Commun.* **2011**, *182*, 978–988.
- (106) Navascués, P.; Obrero-Pérez, J. M.; Cotrino, J.; González-Elipe, A. R.; Gómez-Ramírez, A. Unraveling discharge and surface mechanisms in plasma-assisted ammonia reactions. *ACS Sustainable Chem. Eng.* **2020**, *8*, 14855–14866.
- (107) Khan, N.; Goldberg, D. E.; Pelikan, M. Multi-objective Bayesian optimization algorithm. In *Proceedings of the 4th Annual Conference on Genetic and Evolutionary Computation*; Morgan Kaufmann Publishers Inc., 2002; pp 684.
- (108) Bakshy, E.; Dworkin, L.; Karrer, B.; Kashin, K.; Letham, B.; Murthy, A.; Singh, S. AE A domain-agnostic platform for adaptive experimentation. *Conference on Neural Information Processing Systems* **2018**, 1–8.

- (109) Schulz, E.; Speekenbrink, M.; Krause, A. A tutorial on Gaussian process regression: Modelling, exploring, and exploiting functions. *Journal of Mathematical Psychology* **2018**, *85*, 1–16.
- (110) Emmerich, M. T.; Deutz, A. H.; Klinkenberg, J. W. *Hypervolume-based expected improvement: Monotonicity properties and exact computation*, IEEE Congress of Evolutionary Computation (CEC); IEEE, 2011; pp 2147–2154.
- (111) Smith, R.; Killelea, D.; DelSesto, D.; Utz, A. Preference for vibrational over translational energy in a gas-surface reaction. *Science* **2004**, *304*, 992–995.
- (112) Rouwenhorst, K. H.; Kim, H.-H.; Lefferts, L. Vibrationally excited activation of N<sub>2</sub> in plasma-enhanced catalytic ammonia synthesis: a kinetic analysis. *ACS Sustainable Chem. Eng.* **2019**, *7*, 17515–17522.
- (113) Čadež, I.; Hall, R.; Landau, M.; Pichou, F.; Schermann, C. The influence of a thin gold film on vibrational excitation of hydrogen molecules. *J. Chem. Phys.* **1997**, *106*, 4745–4752.
- (114) Ben Yaala, M.; Saeedi, A.; Scherrer, D.-F.; Moser, L.; Steiner, R.; Zutter, M.; Oberkofler, M.; De Temmerman, G.; Marot, L.; Meyer, E. Plasma-assisted catalytic formation of ammonia in N<sub>2</sub>-H<sub>2</sub> plasma on a tungsten surface. *Phys. Chem. Chem. Phys.* **2019**, *21*, 16623–16633.
- (115) Rouwenhorst, K. H.; Lefferts, L. On the mechanism for the plasma-activated N<sub>2</sub> dissociation on Ru surfaces. *J. Phys. D: Appl. Phys.* **2021**, *54*, 393002.
- (116) van 't Veer, K.; Engelmann, Y.; Reniers, F.; Bogaerts, A. Plasma-catalytic ammonia synthesis in a DBD plasma: role of microdischarges and their afterglows. *J. Phys. Chem. C* **2020**, *124*, 22871–22883.
- (117) Sun, J.; Chen, Q.; Zhao, X.; Lin, H.; Qin, W. Kinetic investigation of plasma catalytic synthesis of ammonia: insights into the role of excited states and plasma-enhanced surface chemistry. *Plasma Sources Science and Technology* **2022**, *31*, 094009.
- (118) Chen, Z. *Investigation of Ammonia Synthesis Assisted by Non-Thermal Plasmas*, Ph.D. Thesis; Princeton University, 2023.
- (119) Patil, B. S.; Cherkasov, N.; Srinath, N. V.; Lang, J.; Ibadon, A. O.; Wang, Q.; Hessel, V. The role of heterogeneous catalysts in the plasma-catalytic ammonia synthesis. *Catal. Today* **2021**, *362*, 2–10.
- (120) Barboun, P.; Mehta, P.; Herrera, F. A.; Go, D. B.; Schneider, W. F.; Hicks, J. C. Distinguishing plasma contributions to catalyst performance in plasma-assisted ammonia synthesis. *ACS Sustainable Chem. Eng.* **2019**, *7*, 8621–8630.
- (121) Chen, S.; Wang, Y.; Li, Q.; Li, K.; Li, M.; Wang, F. A DFT study of plasma-catalytic ammonia synthesis: the effect of electric fields, excess electrons and catalyst surfaces on N<sub>2</sub> dissociation. *Phys. Chem. Chem. Phys.* **2023**, *25*, 3920–3929.